



HAL
open science

Strain partitioning along the anatectic front in the Variscan Montagne Noire massif (Southern French Massif Central)

M. Rabin, P. Trap, N. Carry, K. Freville, Bénédicte Cenki-Tok, C. Lobjoie, P. Goncalves, Didier Marquer

► To cite this version:

M. Rabin, P. Trap, N. Carry, K. Freville, Bénédicte Cenki-Tok, et al.. Strain partitioning along the anatectic front in the Variscan Montagne Noire massif (Southern French Massif Central). *Tectonics*, 2015, 34 (8), pp.1709-1735. 10.1002/2014TC003790 . hal-01208098

HAL Id: hal-01208098

<https://hal.science/hal-01208098>

Submitted on 26 Feb 2018

HAL is a multi-disciplinary open access archive for the deposit and dissemination of scientific research documents, whether they are published or not. The documents may come from teaching and research institutions in France or abroad, or from public or private research centers.

L'archive ouverte pluridisciplinaire **HAL**, est destinée au dépôt et à la diffusion de documents scientifiques de niveau recherche, publiés ou non, émanant des établissements d'enseignement et de recherche français ou étrangers, des laboratoires publics ou privés.



RESEARCH ARTICLE

10.1002/2014TC003790

Key Points:

- Three deformation events formed the Montagne Noire Axial Zone strain pattern
- Partial melting of the gneissic core occurred at 0.65 GPa and 720°C
- Strong strain partitioning occurs along the anatectic front

Correspondence to:

M. Rabin,
mickael.rabin@univ-fcomte.fr

Citation:

Rabin, M., P. Trap, N. Carry, K. Fréville, B. Cenko-Tok, C. Lobjoie, P. Goncalves, and D. Marquer (2015), Strain partitioning along the anatectic front in the Variscan Montagne Noire massif (southern French Massif Central), *Tectonics*, 34, 1709–1735, doi:10.1002/2014TC003790.

Received 24 NOV 2014

Accepted 3 JUL 2015

Accepted article online 14 JUL 2015

Published online 24 AUG 2015

Strain partitioning along the anatectic front in the Variscan Montagne Noire massif (southern French Massif Central)

Mickael Rabin¹, Pierre Trap¹, Nicolas Carry¹, Kevin Fréville², Bénédicte Cenko-Tok², Cyril Lobjoie¹, Philippe Goncalves¹, and Didier Marquer¹

¹UMR 6249 Chrono-environnement, Université de Franche-Comté, Besançon, France, ²UMR 5243, Laboratoire Géosciences Montpellier, Université de Montpellier2, Montpellier, France

Abstract We decipher late-orogenic crustal flow characterized by feedback relations between partial melting and deformation in the Variscan Montagne Noire gneiss dome. The dome shape and finite strain pattern of the Montagne Noire Axial Zone (MNAZ) result from the superimposition of three deformations (D1, D2 and D3). The early flat-lying S1 foliation is folded by D2 upright ENE-WSW folds and transposed in the central and southern part of the MNAZ into steep D2 high-strain zones consistent with D2 NW-SE horizontal shortening, in bulk contractional coaxial deformation regime that progressively evolved to noncoaxial dextral transpression. The D2 event occurred under metamorphic conditions that culminated at 0.65 ± 0.05 GPa and $720 \pm 20^\circ\text{C}$. Along the anatectic front S1 and S2 foliations are transposed into a flat-lying S3 foliation with top-to-NE and top-to-SW shearing in the NE and SW dome terminations, respectively. These structures define a D3 transition zone related to vertical shortening during coaxial thinning with a preferential NE-SW to E-W directed stretching. Depending on structural level, the metamorphic conditions associated with D3 deformation range from partial melting conditions in the dome core to subsolidus conditions above the D3 transition zone. We suggest that D2 and D3 deformation events were active at the same time and resulted from strain partitioning on both sides of the anatectic front that may correspond to a major rheological boundary within the crust.

1. Introduction

Significant crustal partial melting occurs during synorogenic thickening and final stages of collisional orogeny in response to thermal relaxation and mantle to crust heat transfer. Partial melting induces a drastic decrease in strength in the lower and middle crust that changes the orogenic dynamic balance [Vanderhaeghe, 2012]. For instance, gravitational collapse and lateral flow of the crust observed in the Variscan and Himalaya-Tibet belts are interpreted as a consequence of softening of the partially molten deep crust [Schulmann *et al.*, 2008, 2014; Vanderhaeghe, 2009]. This deep partially molten crust is exposed in tectonic windows like “migmatitic gneiss domes,” which are defined by a granitic and migmatitic core mantled by a metamorphic carapace with a high metamorphic gradient. Therefore, migmatitic gneiss domes offer a section of continental crust from shallow to deep structural levels. Among numerous gneiss domes documented around the world, some have been studied in much more detail, like the Thor-Odin dome in the North American Cordillera [Vanderhaeghe and Teysier, 2001; Norlander *et al.*, 2002], the Naxos dome in the Hellenides [Jansen and Schuiling, 1976; Kruckenberg *et al.*, 2011], the Aston-Hospitalet in the French Pyrénées [Denèle *et al.*, 2014], or the Montagne Noire gneiss dome in the French Massif Central [Demange, 1996]. In this paper we focus on the Montagne Noire gneiss dome that has benefited from many studies since the early twentieth century [Bergeron, 1905; Geze, 1940; Gèze, 1949; Marres, 1951; Denizot, 1954; Schuiling, 1960; Collomb and Ellenber, 1965; Debat, 1967; Demange, 1975, 1982, 1999; Hamet and Allegre, 1976; Bard, 1978; Vidal *et al.*, 1980; Thompson and Bard, 1982; Courtillot *et al.*, 1986; Faure and Cottreau, 1988; Echter and Malavieille, 1990; Van Den Driessche and Brun, 1992; Cassard *et al.*, 1993; Aerden, 1998; Soula *et al.*, 2001; Laumonier *et al.*, 2004; Charles *et al.*, 2009; Faure *et al.*, 2010; Poilvet *et al.*, 2011; Rey *et al.*, 2011; Doublie *et al.*, 2014]. Large exposures of unmetamorphosed to weakly metamorphosed upper crust to migmatitic lower crust makes the Montagne Noire a valuable natural laboratory for studying the mechanisms responsible for crustal deformation and in particular the effect of partial melting on orogenic evolution. However, no consensus has yet been reached on the tectonic mechanisms responsible for the origin and the mechanical behavior of the Montagne Noire in this segment of the Variscan orogen. For instance, the

overall tectonic setting at the origin of the building of the gneiss core of the dome is still debated, corresponding to (1) an extensional setting with upper crustal stretching and upward lower crustal flow [Van Den Driessche and Brun, 1992; Franke et al., 2011; Rey et al., 2011] or (2) a synorogenic compressional setting [Aerden, 1998; Demange, 1998; Malavieille, 2010].

The aim of this paper is twofold: (1) to clarify the tectonometamorphic evolution of the Montagne Noire Axial Zone (MNAZ) and (2) to emphasize the role of partial melting on the rheological behavior of the middle crust. Although the MNAZ has been extensively studied, most of the work has concentrated on the eastern part of the core, where exposure is good. Only few studies took into account the western part of the MNAZ [Cassard et al., 1993] or the entire dome structure [Demange, 1999; Charles et al., 2009]. In this paper the whole MNAZ is investigated via a georeferenced data set containing up to 6000 structural data coming from geological maps, published work, and our own field analyses on selected targets. In addition, despite existing petrological works [Bard and Rambelison, 1973; Demange, 1982; Bogdanoff et al., 1984], quantified pressure-temperature (P-T) estimates for the core of the dome as well as its cover are critically lacking. We performed thermobarometric calculations on garnet-cordierite-bearing migmatite located along a N-S trending profile. Particular attention has been paid to the structural setting of each studied sample in order to calculate P-T conditions with respect to deformation and to build P-T-d (deformation) paths. These new results lead to a better understanding of how the Variscan partially molten middle crust behaved during Late Carboniferous time and to a discussion on the role of the anatectic front as a main crustal-scale rheological transition within a mature orogenic crust.

2. Geological Setting

2.1. The Montagne Noire Gneiss Dome Within the Variscan Belt

The Variscan belt is a Late Paleozoic orogen that involved large continental plates (Gondwana, Baltica, and Laurussia) and several Gondwana-derived microcontinents during Early Carboniferous time [Robardet et al., 1990; Matte, 1991, 2001; Tait et al., 1997; von Raumer et al., 2009; Johnston and Gutierrez-Alonso, 2010; Melleton et al., 2010; Franke et al., 2011]. Since the late Visean (circa 330 Ma), intracontinental deformation in the form of wrenching, thrusting, and normal faulting was coeval with intense crustal melting that developed during continental collision [Faure et al., 2009, 2010; Lardeaux et al., 2014].

The Montagne Noire gneiss dome, also called the Montagne Noire Axial Zone (MNAZ), is located at the southern edge of the French Central Massif within the southern external zone of the Variscan belt (Figure 1a). The French Central Massif (FCM) is made of a stack of six main tectonometamorphic units. The uppermost part of the tectonic pile crops out along the northern FCM and consists of the western Thiviers-Payzac/St-Sernin-sur-Rance Unit and the eastern Brévenne Unit that represents the uppermost ophiolitic nappes metamorphosed under greenschist to epidote-amphibolite facies conditions [Faure et al., 2009; Feybesse et al., 1988; Lardeaux et al., 2014]. This ophiolitic domain rests upon a stack of three nappes that are from north to south: (1) the eclogitic to amphibolitic Upper Gneiss Unit, (2) the amphibolitic Lower Gneiss Unit, and (3) the greenschist facies para-autochthonous unit (see Faure et al. [2009] and Lardeaux et al. [2014] for details). South of the para-autochthonous unit (i.e., in the external domain), the French Central Massif consists of a Palaeozoic fold-and-thrust belt bounded to the south by a Visean-Namurian fore-land turbiditic basin [Faure et al., 2009].

The Montagne Noire Axial Zone (Figure 1b) is one of the most typical metamorphic domes recognized in the Variscan Orogen [Géze, 1949] that is specifically positioned within the fold-and-thrust belt unit (Figure 1). Since Géze [1949] and Arthaud [1970], a long-established threefold subdivision describes the Montagne Noire massif (Figure 1b). From north to south, the authors distinguish (1) the northern flank composed of Paleozoic sedimentary sequences [Arthaud, 1970; Aerden, 1998], (2) the Axial Zone (MNAZ) made of gneisses and migmatites forming a dome that is mantled by upper Proterozoic to Ordovician metasedimentary units [Demange, 1993, 1994a; Franke et al., 2011], and (3) a southern flank consisting of a nappe pile that comprises imbricated Paleozoic strata, including a Visean flysch (Figure 1) [Demange, 1996, 1998]. The northern and southern flanks of the dome contain low-grade metamorphic sedimentary sequences of Paleozoic age. These strata are involved in kilometer-scale, late Visean south verging recumbent folds and thrust sheets that are famous for inverted fold limbs developed on a 10 km scale, [Feist and Galtier, 1985]. While these upper crustal domains have been well studied from a structural point of view [Demange, 1993, 1994b, 1998; Franke et al., 2011; Doublie et al., 2014], the analysis of finite strain patterns within the overall axial zone is

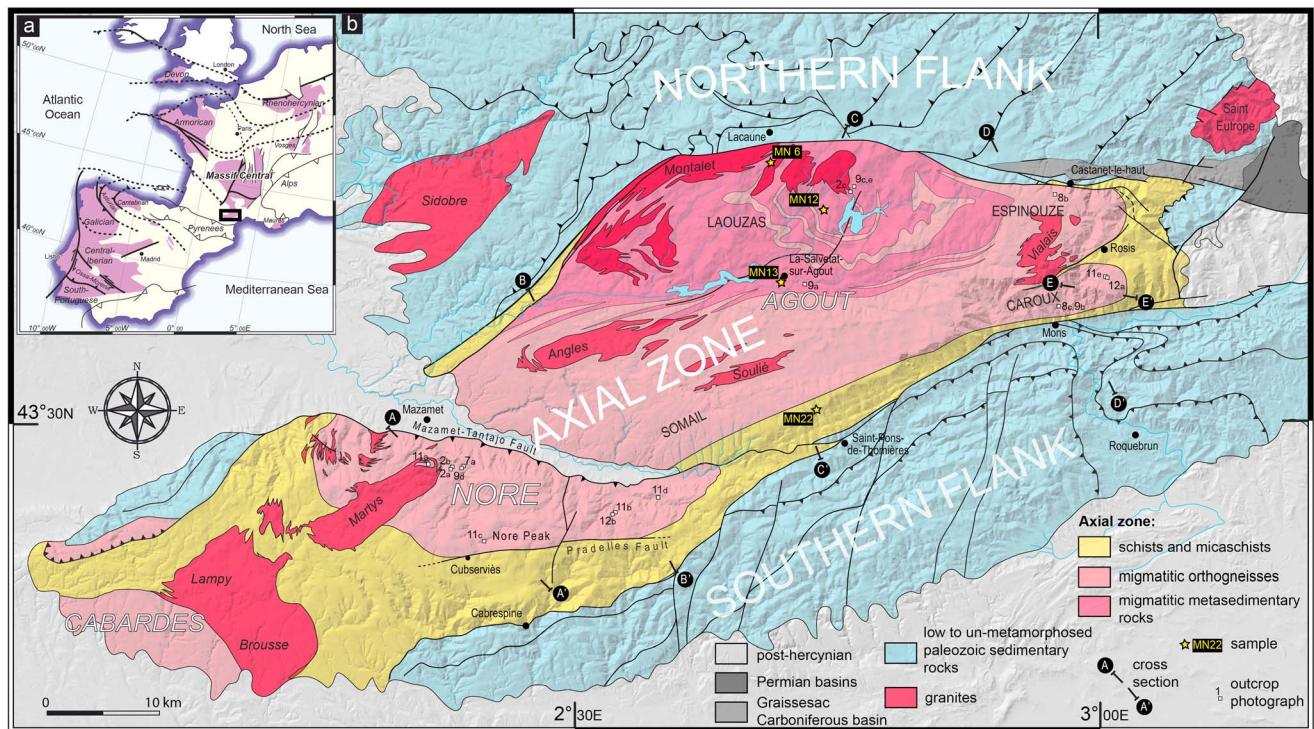


Figure 1. (a) Location of the Montagne Noire massif within the southern part of the French Variscan belt (modified from Ballèvre *et al.* [2012]). (b) Geological map of the Montagne Noire massif: The MNAZ (Montagne Noire Axial Zone). The cross sections of Figures 7, 8, and 10 are located on the geological map (black circles). All the outcrop photographs (white squares numbered with corresponding figure number) and samples (yellow stars labeled MN6, MN12, MN13, and MN22) are also located on the geological map.

lacking. In this paper, we mainly focus on the structurally deepest part of this gneiss dome, i.e., the Montagne Noire Axial Zone (MNAZ).

2.2. Lithology, Ages, and Metamorphism in the MNAZ

The MNAZ is a NE-SW trending gneiss dome made of four main lithological units: (1) schist and micaschist, (2) migmatitic orthogneiss, (3) metapelitic metatexite, and (4) diatexite and granite (Figure 1). The schist and micaschist units envelop the MNAZ and consist predominantly of metapelitic sequences showing a progressive increase of metamorphic conditions from greenschist facies conditions (sericite-chlorite-bearing schist) to amphibolite conditions and andalusite-cordierite-bearing micaschist toward the dome core [Thompson and Bard, 1982]. The migmatitic orthogneiss, also known as the Caroux orthogneiss, makes up the southern part of the MNAZ, from the eastern Caroux to the western Nore dome (Figure 1). The Caroux orthogneiss is an Ordovician metagranite with large K-feldspar phenocrysts that was emplaced at 471 ± 4 Ma and 450 ± 6 Ma (U-Pb zircon ages) within the sedimentary pile that consists of pelite, grauwacke, quartzite, rare volcanics, and carbonate [Alabouvette *et al.*, 2003; Roger *et al.*, 2004; Cocherie *et al.*, 2005]. The Caroux orthogneiss is deformed and shows evidence of synkinematic partial melting (Figures 2a and 8). In the deeper part of the dome, the metatexite of the Laouzas area (Figure 1) formed from a pelitic protolith. Petrological details on these metapelitic metatexites are given in section 4. In the Laouzas-Espinouse area, the metapelitic metatexites are accompanied by leucocratic diatexites corresponding to heterogeneous cordierite-bearing granites such as the Laouzas and Vialais granitoids (Figures 1 and 2b). The emplacement age of these granites remains a matter of debate. U-Th-Pb EPMA (Electron Probe Micro-Analysis) chemical dating of monazite yields an age for the Laouzas granitoid at 327 ± 7 Ma [Be Mezeme, 2005], while U-Pb LA-ICPMS (Laser Ablation Inductively Coupled Plasma Mass Spectrometry) gives an inherited age of 319 ± 2 Ma and an emplacement age at 299 ± 1 Ma [Poilvet *et al.*, 2011]. Two distinct monazite ages were also obtained in the Vialais granites: 327 ± 5 Ma [Matte *et al.*, 1998] and 303 ± 4 Ma [Roger *et al.*, 2015].

Several granites intrude the migmatite and micaschist units of the MNAZ (Figure 1b), and their age of emplacement is controversial. Resolving this issue is beyond the scope of this paper. We concentrate here on the most solid geochronological evidence: the biotite-rich Anglès granite was dated by EPMA dating on

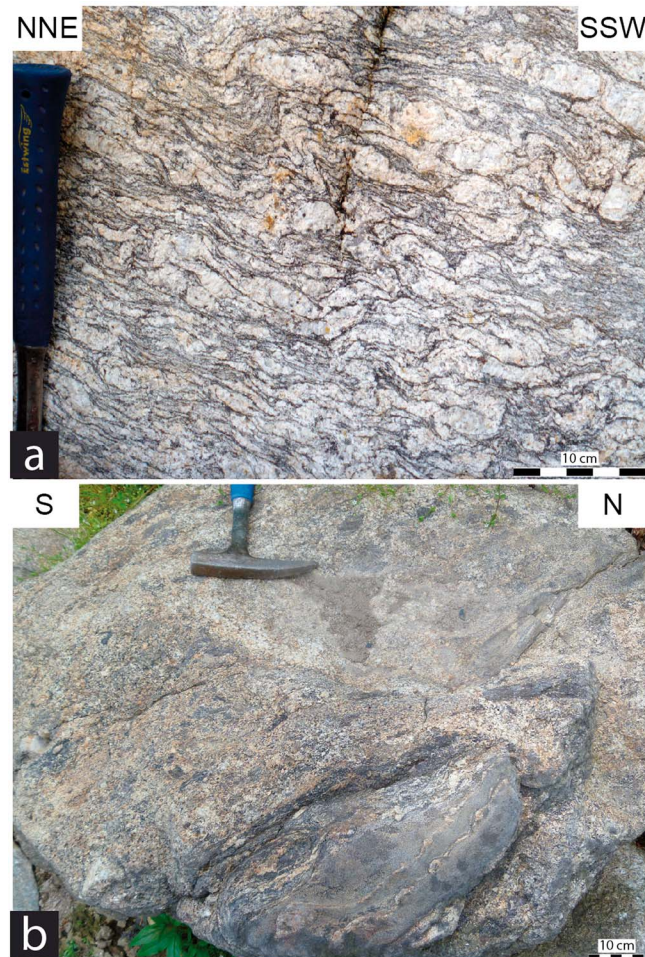


Figure 2. Outcrop photographs of partially molten rocks within the MNAZ. Numbers within white circles correspond to the field location positioned in Figure 1. (a) Migmatitic orthogneiss (metatexite) within the Nore massif (WGS 84: 43.4613°N; 2.38752°E). (b) Migmatitic metasedimentary rocks at the North of Laouzas zone (WGS 84: 43.66153°N; 2.76892°E). Structural data are from this study and from literature [Debat and Mouline, 1979; Collot, 1980; Bogdanoff et al., 1984; Alabouvette and Demange, 1993; Demange et al., 1995, 1997; Aerden, 1998; Soula et al., 2001; Charles et al., 2009].

Demange, 1985; Soula et al., 2001; Alabouvette et al., 2003]. Demange [1985] estimated P-T conditions at 0.9 ± 0.2 GPa and $750 \pm 50^\circ\text{C}$ on the Carbard and Le Jounié omphacite-garnet-quartz-rutile-bearing eclogite. Demange's data were recalculated by Franke et al. [2011] using forward thermodynamic modeling. They obtained minimum peak conditions at approximately 1.4 GPa and 650°C for the same eclogitic rocks. Faure et al. [2014] obtained a Sm-Nd age at 358 ± 9 Ma for the Peyrambert eclogite (near Anglès granite [Demange, 1985]). This eclogite also gave a zircon SHRIMP age at 314 ± 2.5 Ma interpreted as late hydrothermalism [Faure et al., 2014]. Recently, the Terme de Fourcarc eclogite (near Anglès granite) yielded P-T conditions of 1.4 GPa and 725°C and a U-Pb zircon age of 315.3 ± 1.6 Ma interpreted as the age of eclogitization [Teyssier et al., 2015].

The second event M2 shows an abnormal low-pressure/high-temperature (LP-HT) metamorphic gradient up to $50^\circ\text{C}/\text{km}$ that is defined by isograds wrapping around the gneiss core and tightening along the flanks of the dome [Bard and Rambelsson, 1973; Ourzik et al., 1991; Demange, 1996; Soula et al., 2001; Alabouvette et al., 2003]. This M2 event is interpreted as being associated with the exhumation stage of the migmatitic dome, but calculated P-T conditions of migmatitic rocks within the axial core zone are still lacking. Furthermore, P-T conditions of partial melting in the Laouzas migmatite have been estimated at 0.5 GPa

monazite at 325 ± 7 Ma [Faure et al., 2010]. The muscovite + biotite \pm garnet Soulié granite yields an EPMA monazite age at 318 ± 4 Ma [Faure et al., 2010], while two ages at 278 ± 4 Ma and 323 ± 16 Ma were obtained by ID-TIMS (Thermal Ionization Mass Spectrometry Isotopic Dilution) U-Pb dating on zircons [Hamet and Allegre, 1976]. The Martys granite gives a $\text{Rb}^{87}\text{-Sr}^{87}$ whole rock isochron age at 300 ± 34 Ma [Hamet and Allegre, 1976]. The Montalet granite, located along the northwestern edge of the MNAZ, is a biotite- and garnet-bearing peraluminous granite considered as an early plutonic body [Demange, 1996; Alabouvette et al., 2003]. U-Th-Pb EPMA analysis on monazite yields an age at 327 ± 7 Ma [Faure et al., 2010]. For the same granite, Poilvet et al. [2011] gives zircon Th-Pb LA-ICPMS inherited age at 496 ± 15 Ma, three analyses at 323 ± 5 Ma and 16 analyses at 294.1 ± 3.1 Ma. The end of magmatism is marked by several generations of late pegmatite and undeformed granitic dikes that intrude the gneissic rocks of the MNAZ at 292.0 ± 4.4 Ma and 294.3 ± 6.0 , respectively [Collot, 1980; Franke et al., 2011].

Two distinct metamorphic events are documented within the MNAZ. The earliest metamorphic event M1 corresponds to a medium to high pressure event, characterized by the rare occurrence of kyanite-bearing micaschists and boudins of eclogites and garnet-bearing pyroxenites within the migmatitic gneisses [Bouchardon et al., 1979;

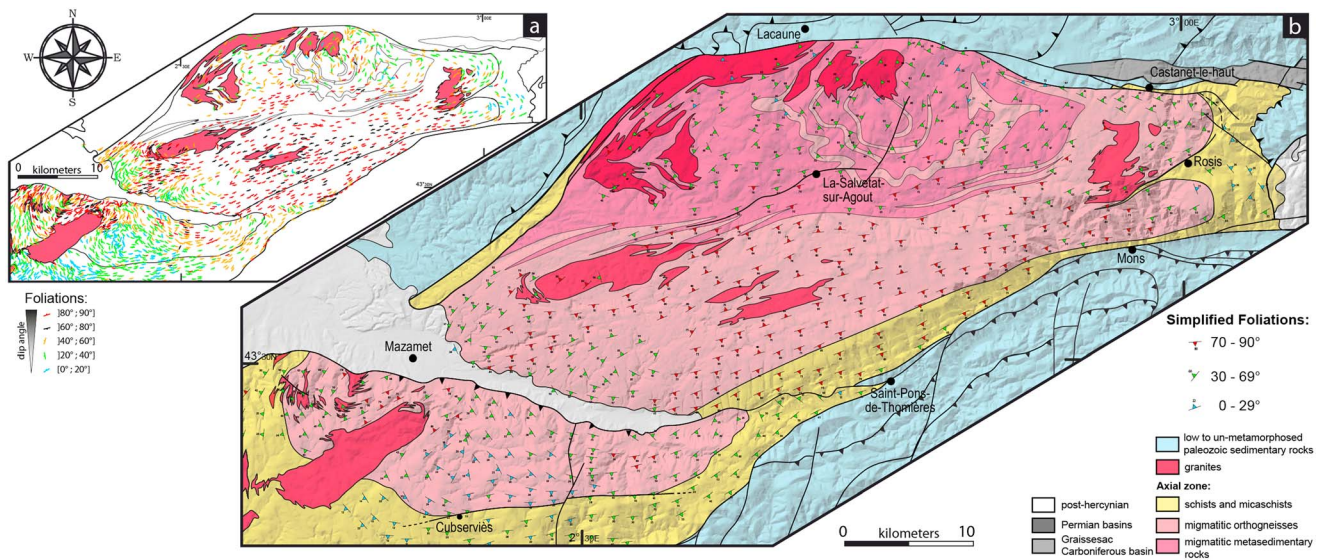


Figure 3. Maps of the MNAZ showing foliation measurements and patterns from our structural geodatabase. (a) Map of georeferenced foliations (WGS 84) from our field measurements and literature compilation (geological maps and field-based data set from BRGM - Bureau de Recherches Géologiques et Minières) sorted by dip angle. (b) Foliation map (WGS 84) resulting from statistical treatment of foliations presented in Figure 3a. Foliations are computed within a 1 km size square as the mean value and the barycenter of the foliations data in each square. The foliations are sorted into three dip angle classes. Large dip angle foliations (70° to 90°) are organized as a N70°E to N80°E directed corridor corresponding mainly to the S2 foliation. Small dip angle foliations (0° to 29°) are mainly located in the uppermost structural levels (S3 foliation). Granites and migmatitic metasedimentary rocks within the Laouzas present moderate dip angle foliations (30° to 69°). Within the Agout area (Caroux, Espinouze, and southwest of Somail) and Nore massif, this medium class highlights S1 upright fold. Structural data are from this study and from literature [Van Den Driessche and Brun, 1992; Brun and Van Den Driessche, 1994; Charles et al., 2009].

and 700°C (M1), and at 0.45 GPa and 620°C (M2) [Ourzik et al., 1991]. Based on new monazite U-Th-Pb_{tot} ages obtained from micaschists and kinzigites, Faure et al. [2014] suggest that the LP-HT M2 metamorphism, coeval with partial melting, occurred during the 340 Ma–320 Ma period. However, Roger et al. [2015] suggest that partial melting and related plutonism occurred between 315 and 300 Ma. Considering the available geochronological data, the ages of both M1 eclogitic and M2 LP-HT metamorphism are not clearly settled yet.

3. Structural Analysis

3.1. Overall Geometry of the MNAZ

The MNAZ bulk geometry is an elongate dome ~90 km long and 20 km wide, with a sigmoidal shape in map view (Figures 1b and 3). The dome outlines a horizontal to gently dipping northern limb, bounded by the ductile Mont de Lacaune Fault, and a steeply southward dipping southern limb, limited by the Mazamet-Tantajo EW trending brittle fault bundle. These brittle fault systems are dominated by late transtensional kinematics [Echtler and Malavieille, 1990; Franke et al., 2011]. The western termination of the dome shows a gently south dipping southern limb and a vertical northern limb. The deepest part of the dome is exposed in the central part of the MNAZ, and the upper structural domains are best observed in the eastern and western pericline terminations and along the southern flank.

The MNAZ is commonly subdivided into two subdomes named the Agout and the Nore domes separated by the Eocene north directed reverse Mazamet Fault (Figure 1b). According to Demange [1998], the Nore dome could have been positioned eastward, south of the Agout dome. The Agout dome is separated into the Laouzas-Espinouze subdome to the north and the Somail-Caroux subdome to the south. The Laouzas-Espinouze subdome represents the deepest level of the MNAZ where intense partial melting led to the generation of cordierite-bearing anatectic granites, like the Laouzas and Vialais granites. The Somail-Caroux subdome mostly consists of partially molten orthogneiss. At the eastern pericline termination, the Espinouze and Caroux subdomes are separated by the Rosis synform that corresponds to a NE trending tight vertical high-strain zone consisting mainly of micaschist.

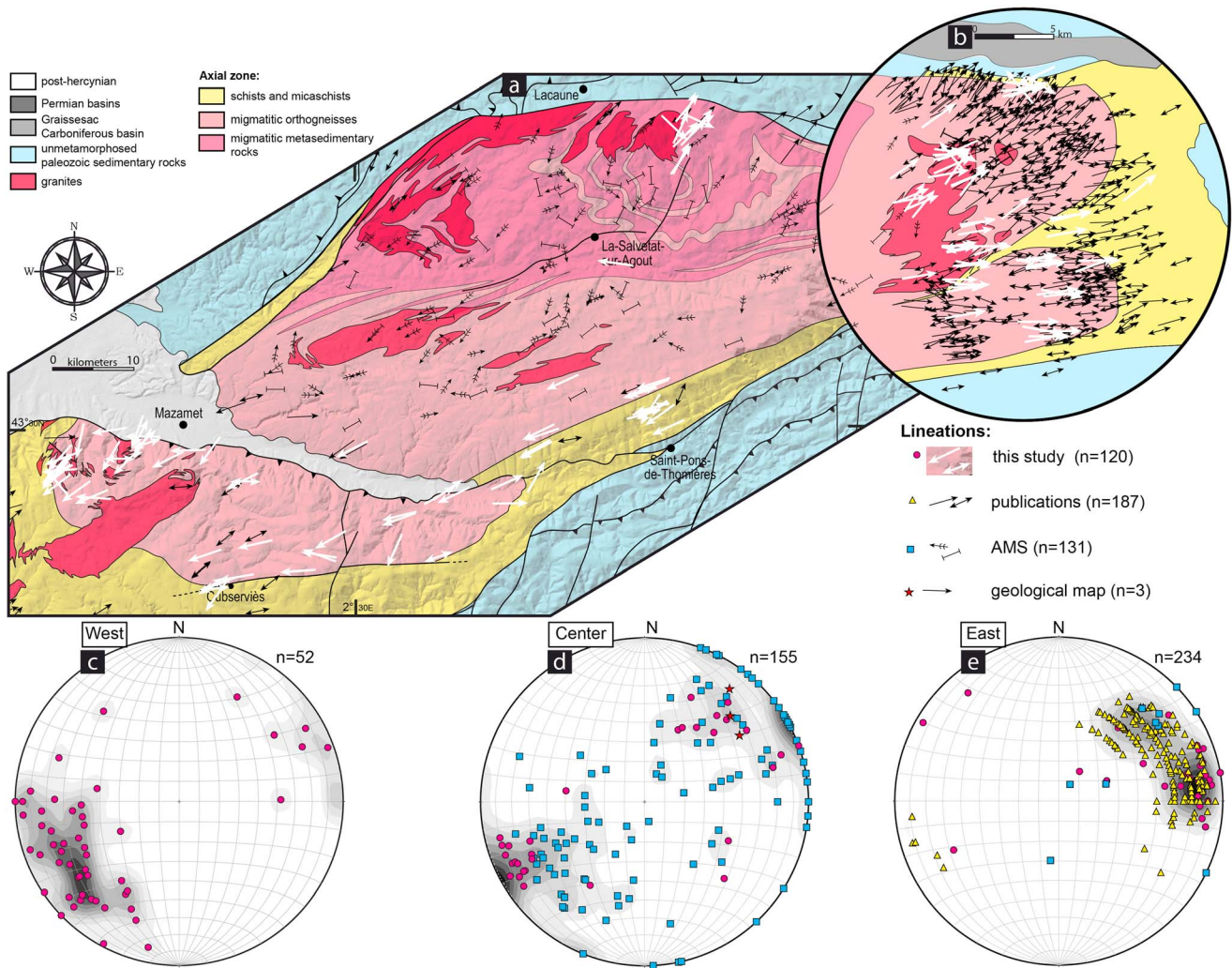


Figure 4. Structural map and poles of foliation planes and lineations plotted in the lower hemisphere of equal-area stereographic projections. (a) Lineation map within the MNAZ from field measurement and literature. Most of the lineations within the center of MNAZ consist of AMS (Anisotropy of magnetic susceptibility) measurements in migmatitic orthogneisses. (b) Zoom on the eastern part of the lineation map where most of the previous studies were performed. (c–e) Stereographic projections corresponding to the western, middle, and eastern parts of the massif. Most of the lineations in MNAZ have a NE-SW orientation (Figures 4a–4c and e). Regarding lineation trend, two classes can be distinguished: northeastward plunge in the NE part (Figures 4b and 4e) and southwestward plunge in the SW part (Figure 4c). AMS data (Figure 4d modified after Charles *et al.* [2009]) present very large dip angle distribution (0° to 80°), whereas most of the field observations have plunge angle smaller than 45°.

Field relationships combined with the multiscale geodata set analysis (Figures 3 and 4) suggest that the finite strain pattern of the MNAZ results from the superposition of three deformation events. Details on the geometry and the kinematics of each deformation event are given by the following sections.

3.2. D1 Deformation

The early S1 foliation is the major planar fabric in both uppermost and lowermost structural domains of the MNAZ. Within the schist and micaschist envelope, S1 dips gently toward the east and the west at the eastern and western dome terminations, respectively (Figures 3, 5a, and 5b). Along the southern internal flank, the S0-S1 foliation is strongly steepened and reworked by the D2 deformation (see hereafter).

In the core of the Nore subdome and mostly around the Laouzas lake, S1 is defined by the preferential alignment of quartzo-feldspathic leucosomes. The S1 attitude is easily depicted and measured within metatextite, while in the Laouzas diatexite and anatectic granites, S1 is defined locally by the preferential orientation of rafts of metasedimentary rocks. In the eastern Espinouse area, S1 is moderately to steeply dipping toward the SE (Figure 3). At the top of the Caroux dome, S1 corresponds to a flat to gently dipping southward

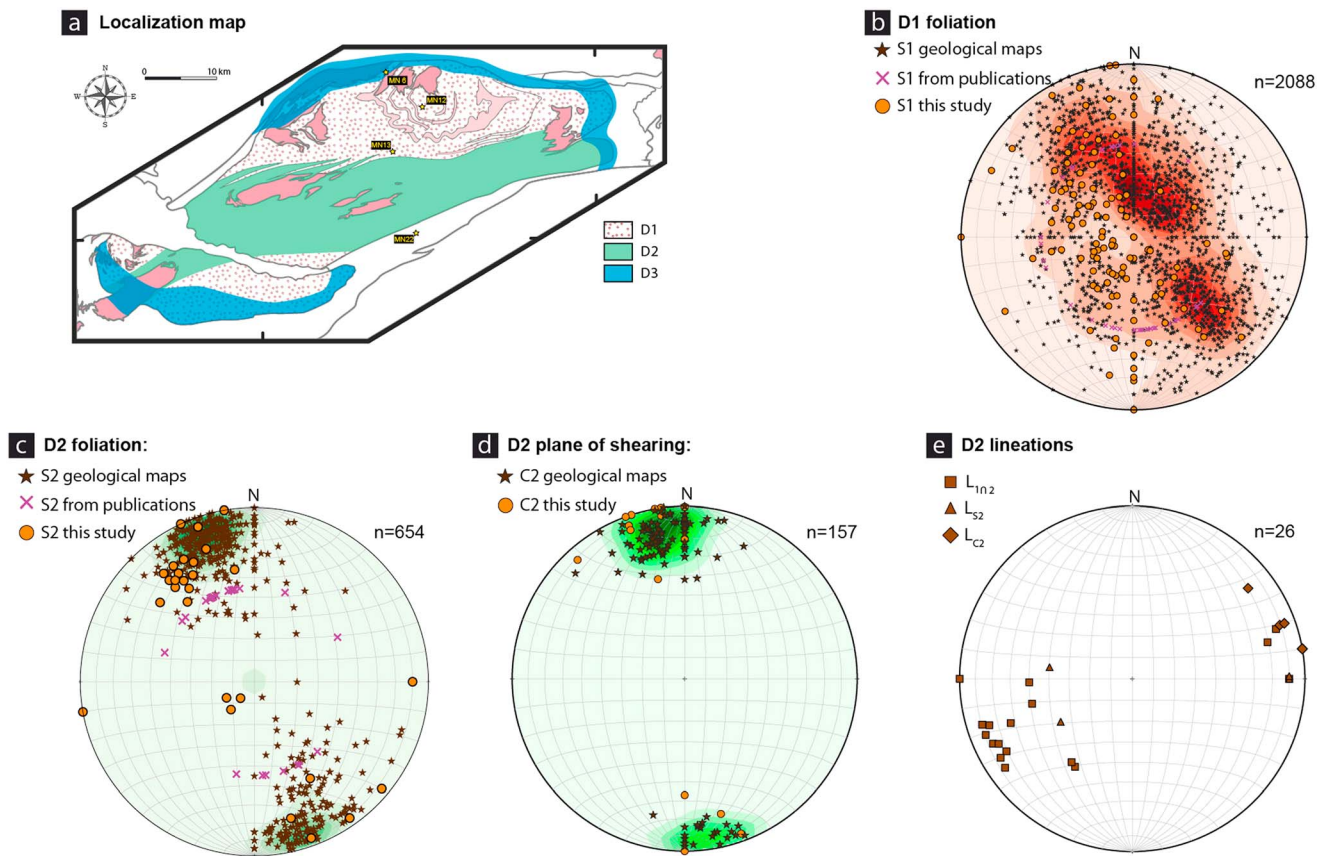


Figure 5. D1 and D2 finite strain patterns plotted in the lower hemisphere of equal-area stereographic projections. (a) Map showing locations of corresponding structural data. (b and c) Poles and density diagram of D1 and D2 foliation planes within the overall MNAZ. (d) Intersection (green square), stretching (green triangle), and crenulation (green diamond) D2 lineations. Most of the D1 and D2 foliations are NE-SW trending and highly dipping (Figures 5b and 5c). The statistic distribution of the poles of D1 schistosity results from a NE-SW folding (density diagram in Figure 5b). The constant azimuth and high dip angle of D2 schistosity define the HSC (Figure 5c). Intersection and crenulation lineations are consistent with NE-SW folding of the S1 (Figures 5b and 5e). Stretching lineations associated with D2 are poorly observed; their overall small plunge is consistent with the transpressive deformation along the HSC.

foliation. In the eastern termination, S1 is folded and subsequently transposed into S3, and interference between S1/S3 and S1/S2 can be observed.

The S1 foliation contains a prominent crenulation lineation, named Lc2, that is related to folding of S1 during NW-SE directed horizontal shortening (D2, Figure 5e). In addition, intersection lineations are reported due to cross-cutting relationships with subsequent D2 ($L1 \cap 2$) and D3 ($L1 \cap 3$) deformations (Figures 4, 5e, and 6c).

3.3. D2 Deformation

D2 deformation is responsible for the large-scale folding of S1 along a broad N50°–N70° trending subhorizontal axis with a subvertical axial plane (Figures 7 and 8). At a smaller scale, the geometry of F2 folds changes depending on D2 intensity and pre-D2 S1 attitude. Where the early S1 envelope is flat lying, F2 folds correspond to symmetrical open to tight folds locally accompanied by the development of a subvertical axial planar cleavage (S2). More commonly, F2 folds are asymmetric and correspond to subordinate folds of larger decameter- to kilometer-scale F2 folds (Figure 7). Anatectic melts and pegmatites commonly intrude parallel to the S2 foliation (Figure 9a). The D2 axial plane crenulation cleavage is difficult to observe owing to metamorphic recrystallization and annealing (Figure 9b).

D2 deformation is strongly localized in a major N70° trending 10 km wide high-strain zone located between the Nore dome and the Laouzaz/Espinouse subdomes and called the D2 high-strain corridor (HSC) (see cross sections in Figures 7 and 8). In this HSC, deformation is heterogeneous and characterized by a network of anastomosed S2 foliation wrapping around lens-shaped domains where S1 is preserved (Figure 7b). In the

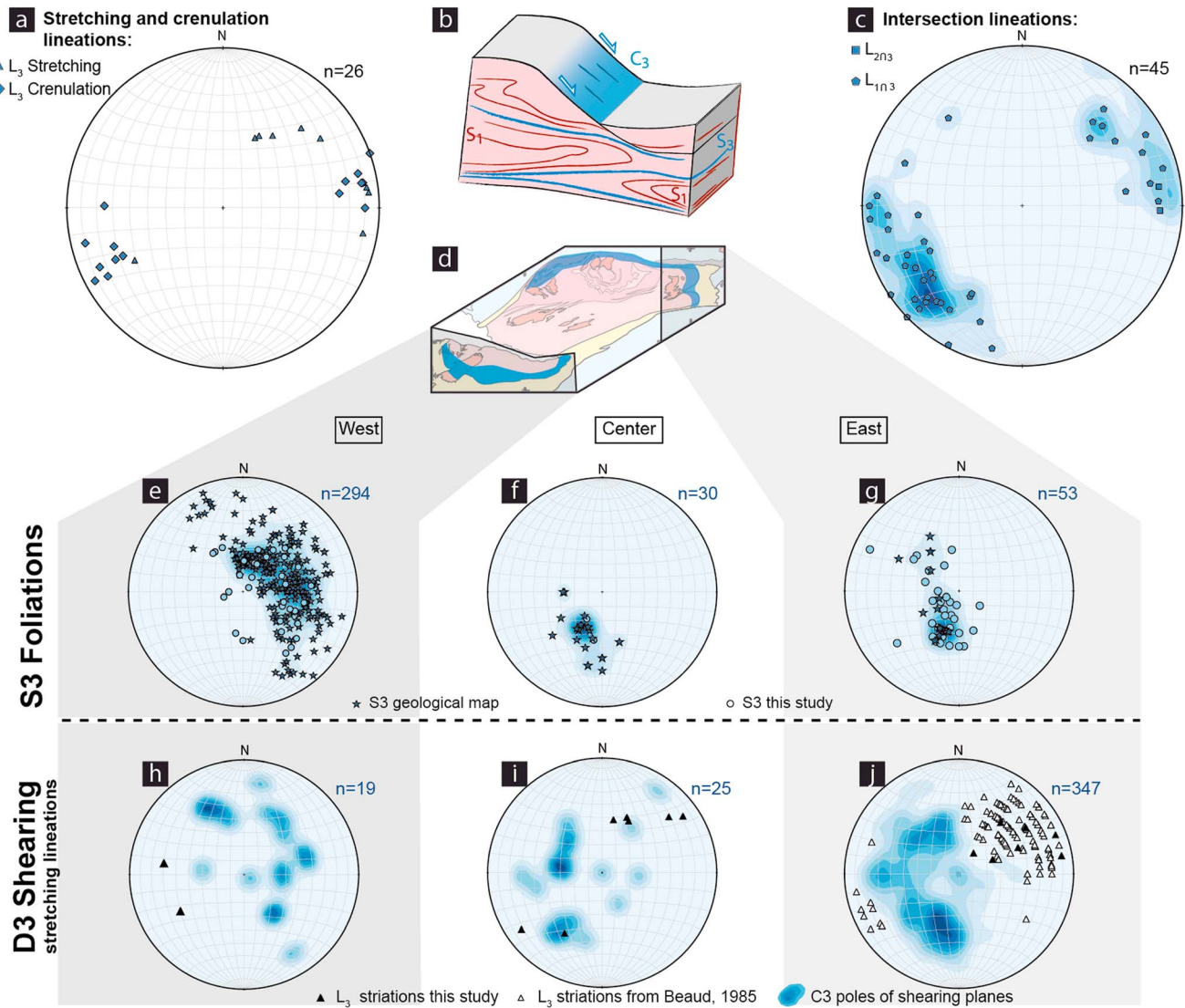


Figure 6. D3 finite strain patterns plotted in the lower hemisphere of equal-area stereographic projections. (a) Stretching and crenulation L3 lineations within the overall MNAZ. (b) Three-dimensional sketch of the vertical shortening during D3. (c) Intersection lineations between S3 and S2 (L_{2n3}) and S3 and S1 (L_{1n3}) within the overall MNAZ. (d) Map locating the spatial extension of D1, D2, and D3 strain patterns. (e–g) Poles and density diagrams of the S3 foliations within the Nore Dome and central part and eastern part of the Agout Dome. (h–j) Density diagrams of the pole of C3 shearing planes (n value corresponds to the number of poles) and associated L3 within the Nore Dome and central part and eastern part of the Agout Dome. D3 strain pattern is weakly plunging toward the east and the west in the eastern and western part of the MNAZ, respectively (Figures 6a, 6c–6e, 6g, 6h, and 6j). The S3 corresponds to a moderately dipping planar fabric, occurring in the uppermost structural levels (Figures 6e–6g). D3 strain pattern only occurs north of the central part of the MNAZ (Figures 6d, 6f, and 6i). The S3 is affected by late C3 shear bands presenting a top-to-the-east and top-to-the-northeast shearing in the eastern part and symmetrically a top-to-the-west and top-to-the-southwest shearing in the western part of the MNAZ (Figures 6h–6j).

highest strain domains S1 is completely transposed into a near-vertical penetrative S2 foliation. Within the D2 HSC, metric to decametric lenticular bodies of syn-D2 granites show a magmatic planar fabric parallel to the S2 foliation. The S2 foliation holds a L2 biotite-bearing mineral lineation that plunges shallowly toward the west and east (Figure 5e). In the western part of the HSC, both fold axes and lineations show a predominant westward plunge, while in the eastern portion of the HSC these structures plunge toward the east.

The occurrence of shallowly plunging lineations associated to the sigmoidal pattern of S1 and S2 in map view is consistent with a dextral shearing component (Figure 10). Within the HSC, and more particularly at the center of the Agout dome, S2 foliation evolves continuously to a $N80^{\circ}$ – $N90^{\circ}$ direction that corresponds to a kilometer-scale dextral D2 shear zone (Figures 3, 5d, and 10). At outcrop scale, kinematic criteria like σ -clasts, subvertical D2 shear bands striking 80° N– 90° E, and drag folds also reveal a dextral shear component in the

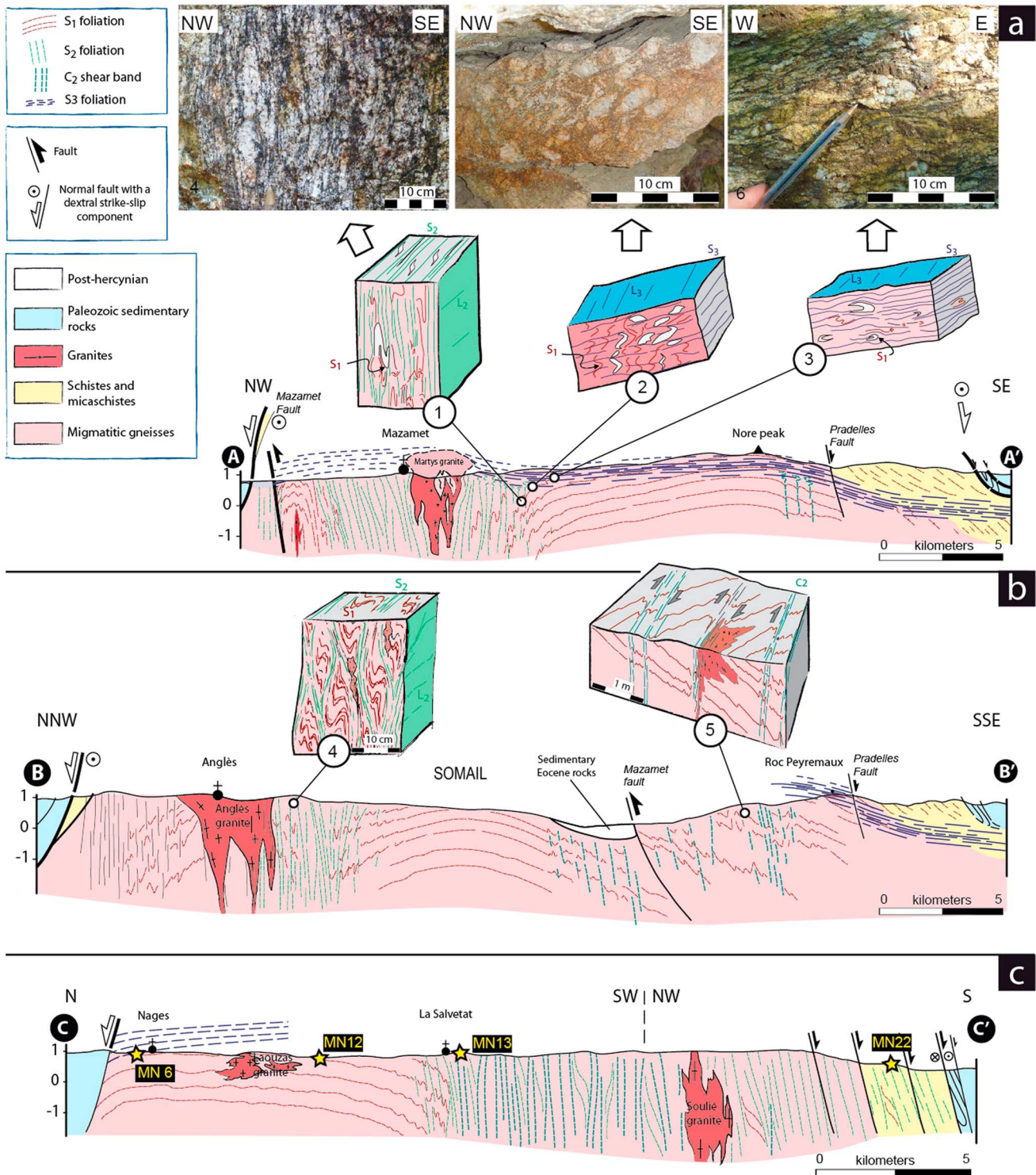


Figure 7. Cross sections through the MNAZ. From west to east: (a) NW-SE trending cross section through the Nore dome. (b) NNW-SSE trending cross section through the western part of the Agout dome. (c) N-S trending cross section through the central part of the Agout Dome with locations of samples presented in the petrological section. Sketches 1 to 3 and associated outcrop photographs (WGS 84: 43.46269°N; 2.39966°E) present field observations along the cross section AA'. Sketches 4 and 5 present field observations along the cross section BB'. In cross section AA', the S1 presents a double dome shape with NE-SW axes. The two domes are separated by a penetrative vertical S2 (HSC) along which the Martys, Anglès, and Soulié granites intrude the migmatitic gneisses. The uppermost structural levels correspond to a subhorizontal S3 schistosity that reworked both S1 and S2.

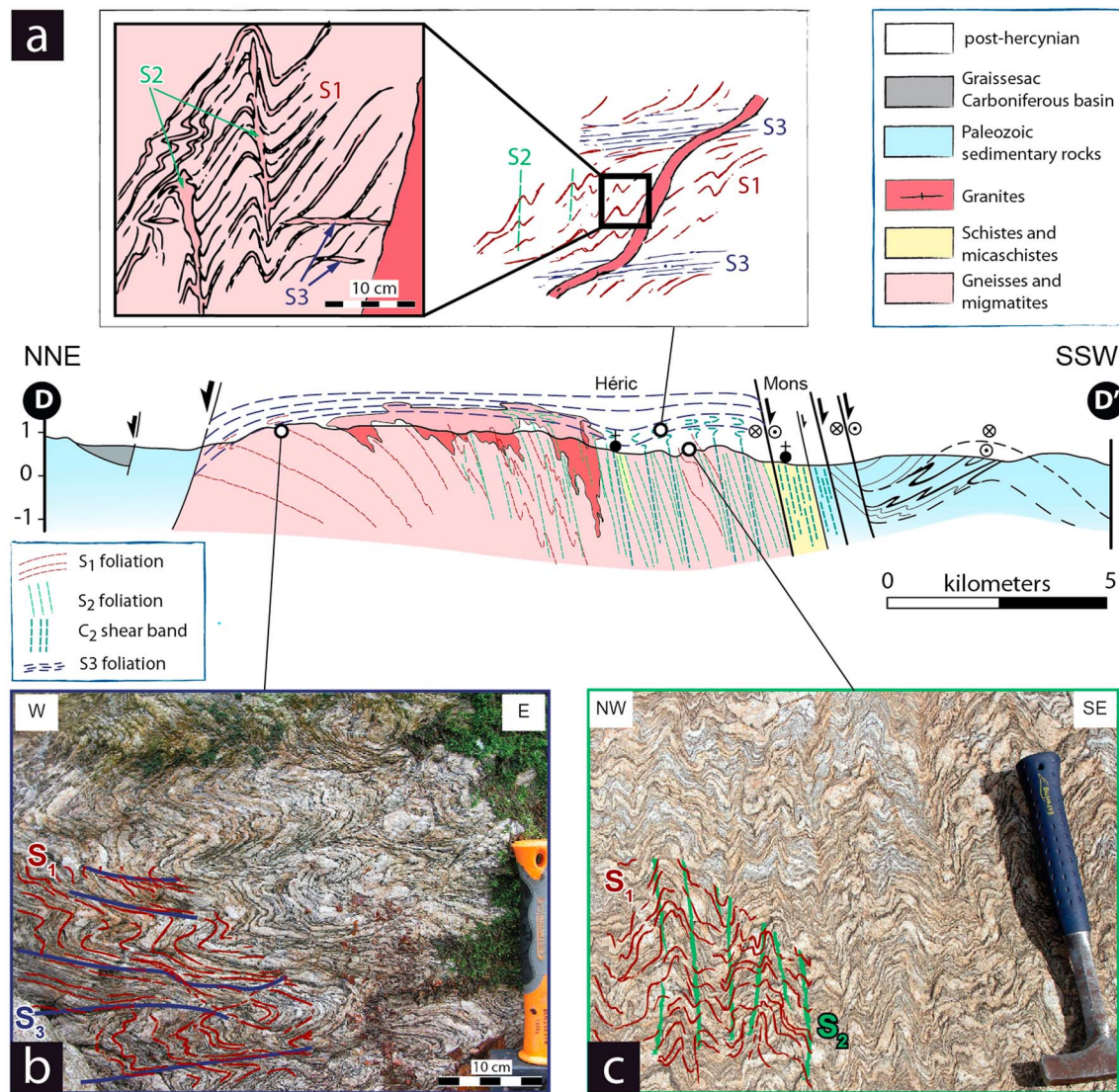


Figure 8. Cross sections through the eastern part of the MNAZ. (a) NNW-SSE trending cross section through Espinouze and Caroux subdomes. Sketches illustrate the relationships between D1, D2, and D3 strain patterns. (b) Outcrop photograph illustrates the relationships between D1 and D3 strain patterns (WGS 84: 43.660002°N; 2.964057°E). (c) Outcrop photograph illustrates the relationships between D1 and D2 strain patterns (WGS 84: 43.65807°N; 2.96123°E).

middle part of the dome (Figures 11a and 11b). In map view, the elongated shape of the Soulié and Anglès granites parallel to the S2 foliation as well as the asymmetrical shape of the Anglès granite suggest that these intrusives were syntectonic, synchronous with D2 deformation (Figure 10). Although the dextral component of D2 deformation dominates, local sinistral shear criteria are observed, in particular along the southern gneiss-micaschist boundary [Faure and Cottreau, 1988; Van Den Driessche and Brun, 1992; Charles et al., 2009; Franke et al., 2011] and within the Rosis high-strain zone [Beaud, 1985].

The southern limit of the HSC bounds the northern part of the Somail and Nore subdomes (Figures 7a and 7b). To the west, in the Nore massif, S1 foliation marks a NE-SW trending synform, here called the Martys synform, intruded by the Martys granite (Figure 7a). The southern edge of the D2 HSC is NE-SW trending because S2 predominates, while in the northern part of the HSC, the E-W trend dominates, controlled by the predominance of D2 shear bands (Figures 7c and 10). The northern limit of the HSC coincides with the southern boundary of the Laouzas-Espinouze subdomes (Figures 7c and 8a). Eastward and up section, the HSC ends with the Rosis synform that is intruded by the Vialais granite. Both Martys and Rosis synform are evidence for D2 horizontal shortening.

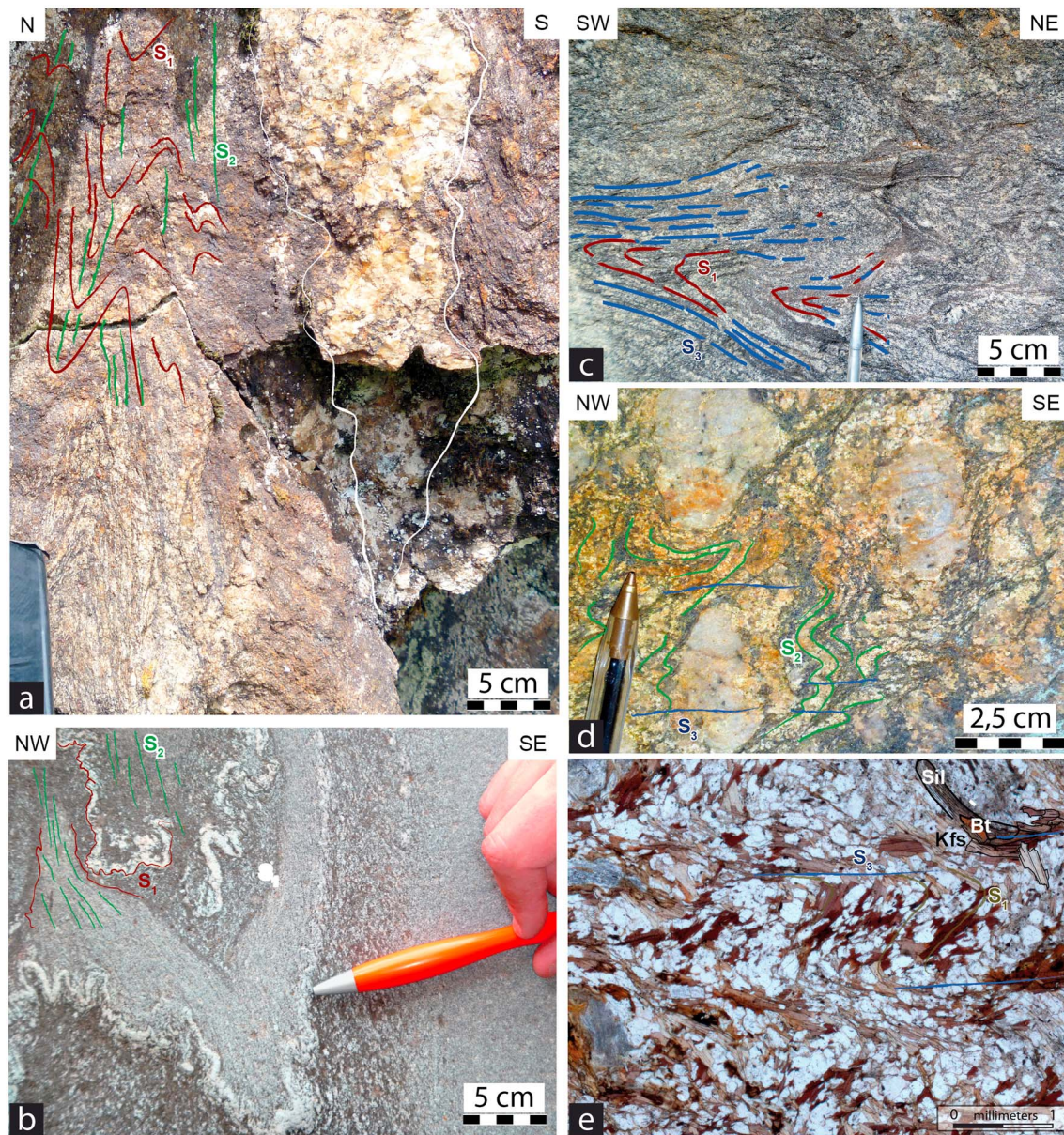


Figure 9. Outcrop photographs of strain pattern of D2 and D3. (a) Migmatitic S1 folded by N-S shortening (D2) with pegmatite located within the axial planar fabrics (WGS 84: 43.59885°N; 2.71021°E). (b) Gradient of deformation through the flat S3 foliation. K-feldspar is increasingly deformed (horizontal flattening) toward the lower part of this S3 zone (WGS 84: 43.45882°N; 2.63233°E). (c) Folded S1 transposed by the flat S3 foliation (WGS 84: 43.66494°N; 2.77120°E). (d) Vertical foliation (S1-2) transposed by the flat S3 foliation (WGS 84: 43.46179°N; 2.40210°E). (e) microphotography of thin section showing high temperature conditions (Sil Bt, Kfs bearing assemblage) of D3 (WGS 84: 43.6727°N; 2.77647°E). Mineral abbreviations are from Kretz [1983].

3.4. D3 Deformation

D3 fabrics are restricted to a ~2–3 km thick zone that affects the upper level of the MNAZ, along the migmatite/micaschist boundary. D3 deformation is observed on both eastern and western dome terminations and along the northern part of the MNAZ, where S3 foliation dips weakly to moderately toward the east and the west, respectively (Figures 6–8). In low D3 strain domains, S3 foliation corresponds to the axial plane of F3 folds with shallow to horizontal dips and NE-SW to E-W trending fold axes. The progressive development of S3 foliation proceeds from F3 folding of S1 and S2 to subsequent transposition (Figures 7, 8, and 9c–9e). The D3 strain gradient is well depicted along a NW-SE cross section within the Nore dome where one can observe discrete, near-horizontal S3 schistosity within open F3 folds evolving toward a complete transposition of S2 by S3 foliation (Figure 7a). In the northeastern region of the Espinouse subdome, it is

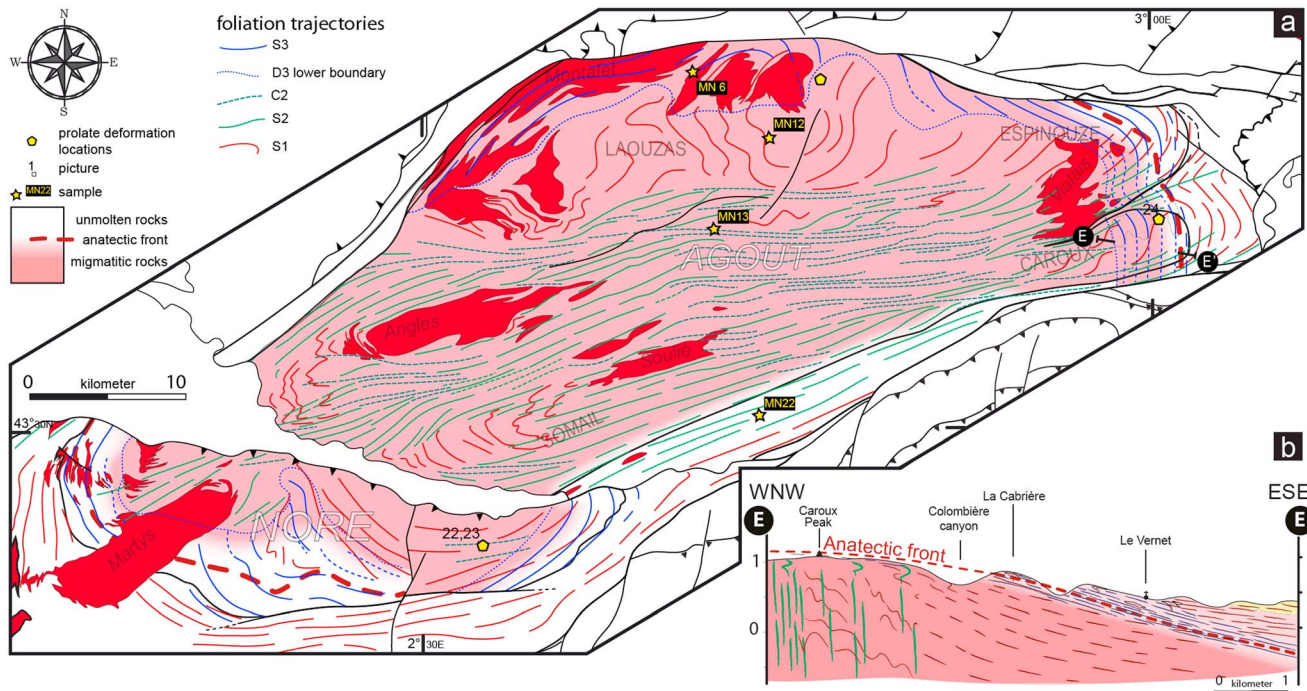


Figure 10. (a) Interpretative map showing foliation trajectories that highlight the strain partitioning between D1, D2, and D3. The early S1 foliation (red lines) is affected by a E-W to NE-SW D2 folding that is still observable in the north part of the Agout dome and at the eastern and western dome pericline zones. The D2 deformation concentrated along a NE-SW directed steeply dipping high-strain corridor (HSC, green lines). The S2 is lately affected by E-W directed dextral C2 shears (dark green lines). Along the northern side of the Agout dome as well as at the eastern and western endings of the migmatitic core (Espinouze-Caroux massifs and Nore massif, respectively) the D3 deformation occurs as a flat-lying S3 foliation (S3, blue lines). Yellow pentagons correspond to outcrop locations where L-type tectonites have been reported and shown in Figure 12. (b) E-W trending cross section through the eastern part of the Caroux sub-dome. The D3 transition zone occurs in the anatectic front transition zone (AFTZ).

the S1 foliation that is folded by F3 folds with axial planes dipping to the NE (Figure 8). In the highest D3 strain zones, S1 and/or S2 are completely transposed into a newly formed S3 foliation.

A NE-SW trending L3 intersection lineation between S1 and S3 is locally observed on S3 foliation planes as well as a L3 crenulation lineation on S1 and S2 surfaces (Figures 6a and 8b). In the uppermost levels and highest D3 strain zone, S3 foliation holds a NE-SW trending L3 stretching lineation. Depending on S3 attitude, L3 lineations plunge toward the NE and the SW at the eastern and western edge of the dome, respectively (Figure 6). Kinematic criteria are also documented by shear bands and C/S fabrics that develop within orthogneisses at subsolidus state (Figures 11c–11e). Along D3 shear bands, a normal and top-to-the-east and NE sense of shear is documented in the eastward termination of the Espinouse and Nore massifs as well as in the middle part of the Agout dome (Figures 6 and 11c–11e). A normal and top-to-the-west shearing is documented in the western Nore dome. Similar to S3 planar fabrics, the D3 shear surface envelope is folded by F2-like upright folds with a N70° trending axial plane and gently plunging axes (Figure 6j).

The general orientation of the S3 foliation and kinematic criteria are consistent with vertical shortening. However, S3 foliation is also affected by low-amplitude upright open folds with E-W trending fold axis. At outcrop scale, this folding mainly leads to a crenulation lineation on the S3 foliation with an E-W trending direction (Figure 6a). This late buckling is consistent with a north-south horizontal shortening contemporaneous with vertical shortening.

The gently dipping S3 foliation surfaces observed along the northern, eastern, and western edges of the dome are defined as a distinctive, flat-lying enveloping carapace, the base of which is called the S3 transition zone. This transition zone separates two domains of distinct metamorphic grade. Below the S3 transition zone, rocks consist of metapelitic garnet-cordierite-bearing metatexite as well as migmatitic orthogneiss. Above the S3 transition zone, rocks do not show any evidence of partial melting (Figures 8a and 8b). At the kilometer scale and beneath the S3 transition zone, the gradual transposition of the HSC into the flat-lying S3 transition zone can be observed. In this scheme, the architecture of the Rosis synform and the Martys synform are similar. Typical fabrics resulting from the interference patterns between S1, S2, and S3 correspond to

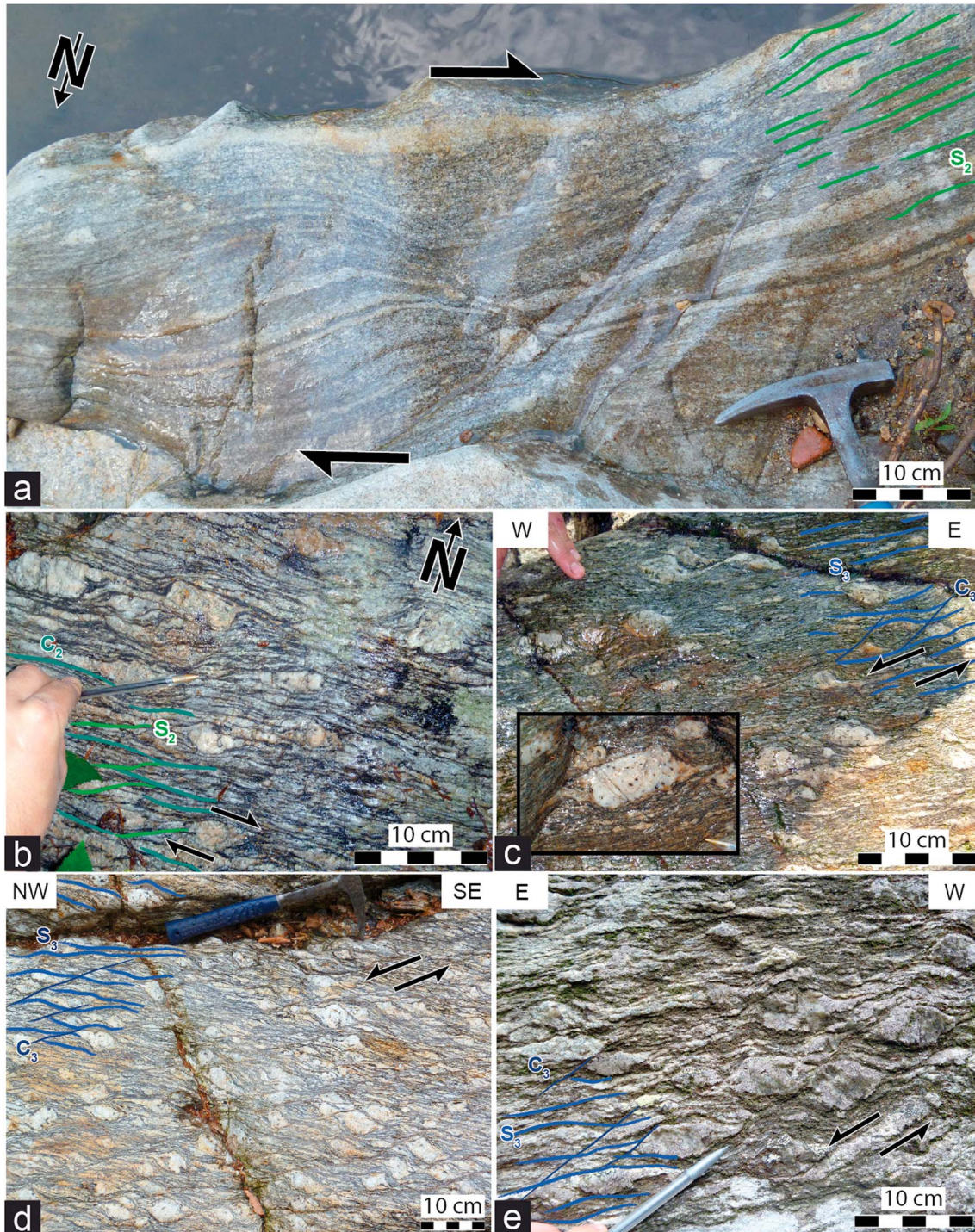


Figure 11. Outcrop photographs of kinematics criteria for D2 and D3. The numbers in white circles correspond to the field location positioned in Figure 1. (a) Migmatitic, NE-SW directed steep foliation (S_2) affected by E-W shear plane (C_2) showing a dextral sense of shear in the Nore dome (WGS 84: 43.47591°N; 2.3729°E). (b) Dextral shearing sense in a migmatitic E-W directed steep foliation (S_2) in the Nore dome (WGS 84: 43.43964°N; 2.5295°E). (c) Sigmoid shaped K-felspar showing a top-to-the-west shearing sense within a subhorizontal foliation (S_3) in the Nore dome (WGS 84: 43.42510°N; 2.40735°E). (d) Top-to-the-west shear criteria within the subhorizontal S_3 foliation at the top of the Nore dome (WGS 84: 43.45041°N; 2.58792°E). (e) Top-to-the-east shear criteria within the subhorizontal S_3 foliation at the top of the Caroux dome (WGS 84: 43.60996°N; 3.00906°E).

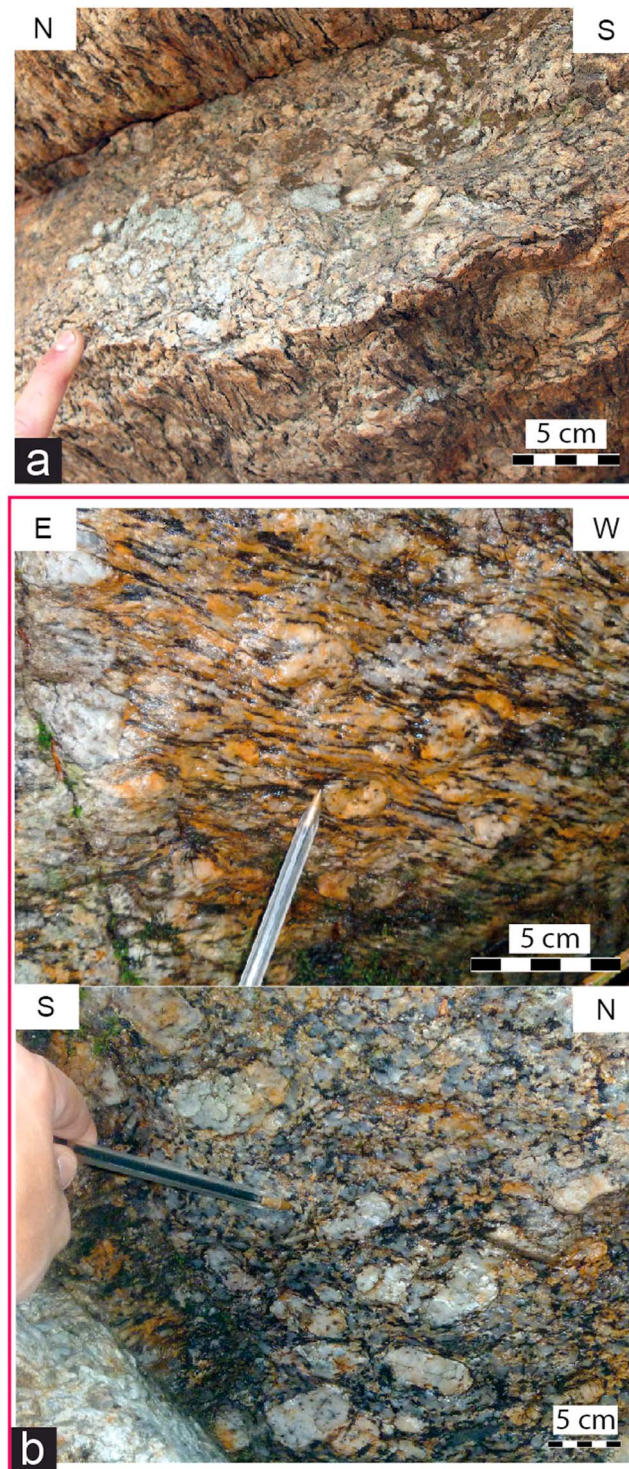


Figure 12. Outcrop photographs showing (a) L-type strain pattern resulting from S1/S3 at the top of the Caroux dome (24; WGS 84: 43.60996°N; 3.00906°E). (b) Constrictional fabric in a syntectonic granite within the transition D2/D3 in the Nore dome (top x/z view and bottom x/y view. WGS 84: 43.43964°N; 2.5295°E).

linear-fabric tectonites that are preserved at several localities along the lower S3 transition zone (Figures 10 and 12a). Some granites intruding along the S3 transition zone show a strong constrictional fabric resulting from the presumed coeval nature of D2 and D3 (Figure 12b).

4. Petrological Analysis

In this section, we present thermodynamic modeling for four metamorphic rocks along a N-S trending profile in the central part of the MNAZ. Three samples of well-preserved garnet-sillimanite-cordierite pelitic metatexite (MN6, MN12, and MN13) were sampled in the middle part of the MNAZ within S1, S2, and S3 domains, respectively (Figures 1 and 7c). In addition, a staurolite-bearing garnet micaschist (MN22) was sampled in the southern flank near St Pons (Figures 1 and 7c). Bulk rock compositions (Table 1) were obtained through WD-XRF (Wavelength Dispersive X-Ray Fluorescence) analysis at University of Lausanne, Switzerland. Electron microprobe analyses were performed on a CAMECA SX100 at the University of Lille, France. Results are presented in Table 2.

4.1. Samples Petrography and Mineral Chemistry

The pelitic metatexite samples MN6, MN12, and MN13 all consist of a medium-grained, quartz-K-feldspar-plagioclase-biotite-sillimanite matrix with garnet and/or cordierite porphyroblasts. Cordierite appears as coronas around garnet porphyroblasts (Figure 13).

In sample MN6 garnet porphyroblasts appear as pseudomorphs and are entirely transformed into cordierite. Cordierite is homogeneous in composition with $X_{Fe} = 41\%$ (Table 2) and is frequently associated with sillimanite and biotite. Two generations of biotite can be distinguished based on textural relationships with a primary, matrix-forming biotite. Secondary biotite appears either as elongated crystals around quartz-cordierite-sillimanite

Table 1. Bulk Chemical Composition in Weight Percent Oxides for Samples MN6, MN12, MN13, and MN22

Sample	SiO ₂ wt %	Al ₂ O ₃ wt %	Fe ₂ O ₃ wt %	K ₂ O wt %	MgO wt %	Na ₂ O wt %	TiO ₂ wt %	CaO wt %	MnO wt %	P ₂ O ₅ wt %	LOI wt %	Total wt %
MN6	51.41	20.96	10.95	4.68	4.03	1.91	1.41	0.69	0.12	0.10	3.35	99.60
MN12	56.28	22.16	9.93	2.83	2.62	1.20	1.03	0.58	0.22	0.10	3.08	100.03
MN13	59.73	18.65	8.38	3.17	2.96	1.72	1.13	1.20	0.11	0.21	2.77	100.02
MN22	65.61	17.07	6.82	3.00	2.77	0.44	0.78	0.08	0.06	0.07	3.29	99.97

nodules or as rounded crystals within in these nodules (Figure 13). Biotite crystals show similar chemical compositions independent of their textural position (XBtFe = 59%, Table 2). Within MN6, S3 defines the axial planar fabric of F3 folds (F3 fold S1) with no difference in mineral assemblage between the S1 and S3 fabrics.

In samples MN12 and MN13, garnet porphyroblasts are inclusion-poor, and garnet- or cordierite-quartz intergrowths are not observed. The composition of garnet cores range from 69% to 75% almandine, 3% to 5% grossular, 6% to 12% spessartine, and 11% to 18% pyrope. Garnet is frequently partially transformed into cordierite. All biotite grains are similar in composition and are chemically homogeneous (Table 2). The crystallization of cordierite in biotite-sillimanite rich domains is also visible. The abundance of primary biotite and absence of muscovite suggest that (i) melting occurred after muscovite breakdown reaction (see phase diagram modeling in section 4.2) and (ii) garnet porphyroblasts are not peritectic but inherited from amphibolite facies prograde metamorphism.

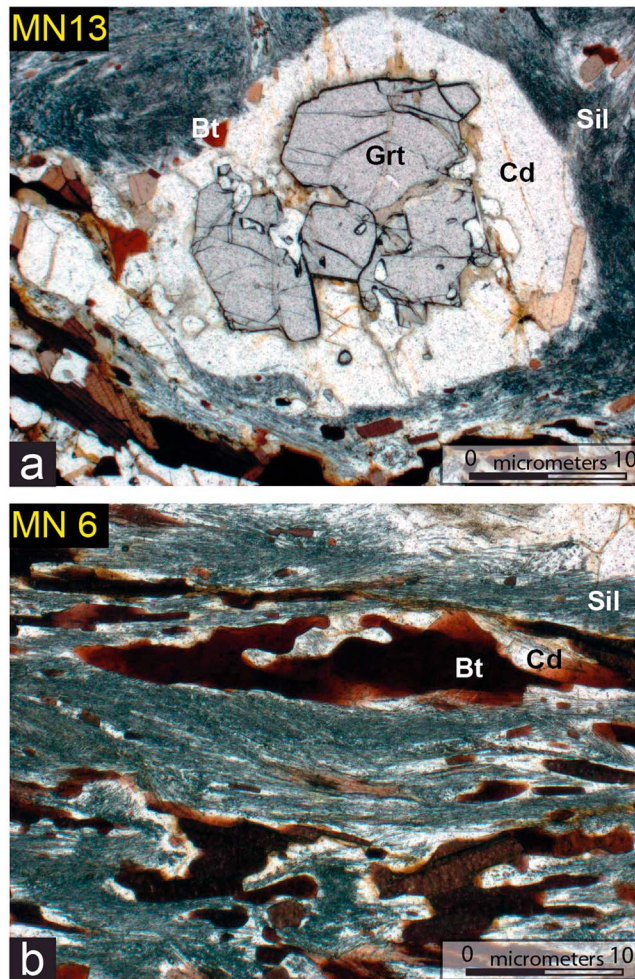


Figure 13. Representative microphotographs of migmatitic metapelites. (a) Cordierite coronas around garnet that proceeds from crystallization during decompression (sample MN13—WGS 84: 43.60144°N; 2.70598°E). (b) Cusped biotites separated from sillimanites by cordierites (sample MN6, WGS 84: 43.68558°N; 2.70027°E) showing incipient biotite destabilization by reaction with sillimanite, plagioclase and quartz to form cordierite, K-felspar, and melt.

Sample MN22 is a staurolite-bearing garnet micaschist. The S1-2 planar fabric is defined by preferential alignment of micas and quartz ribbons. Considering the porphyroblasts location within the rock fabrics, the garnet-staurolite-bearing equilibrium assemblage may correspond to the D1 event without visible reequilibration during D2 deformation. Garnet porphyroblasts (1 mm to 3 mm in size) are euhedral to subhedral and show compositional changes from core to rim (Table 2). Subhedral 50 mm to 100 mm size staurolite grains are chemically uniform irrespective of their textural position, with a constant Mg content and XFe around 82%. Biotite chemical composition shows 67% annite component (Table 2).

4.2. Thermobarometric Modeling

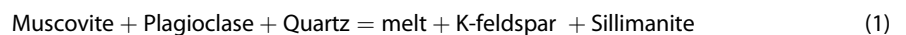
Phase relations were modeled in a nine-component MnO-Na₂O-CaO-K₂O-FeO-MgO-Al₂O₃-SiO₂-H₂O (MnNCKFMASH) system. Pseudosections were calculated with Perple_X'6.6.7 [Connolly and Petrin, 2002; Connolly, 2005] using rock-specific bulk compositions. Thermodynamic data of end-members are from the updated version of the internally consistent thermodynamic database of Holland and

Table 2. Representative Chemical Compositions of Minerals Used for Thermobarometric Calculations

	Garnet				Biotite				Cordierite			Staurolite		
	12A		13A		22A		6A	12A	13A	22A	6A	12A	13A	22A
	core	rim	core	rim										
wt %														
SiO ₂	36.74	36.44	36.95	36.62	38.04	35.27	34.66	34.52	36.26	48.9	46.55	47.47	28.23	
TiO ₂	0.06	0	0.05	0.04	0.11	3.75	4.07	3.29	1.57	0	0.05	0.03	0.27	
Al ₂ O ₃	21.09	20.94	21.33	21.08	21.06	19.31	18.99	18.84	19.87	32.94	31.35	32.1	54.44	
FeO	32.22	34.2	31.27	33.49	32.23	19.34	21.92	21.38	17.55	9.4	12.28	10.08	13.37	
MgO	3.16	3	4.63	3.53	2	7.64	6.15	7.52	10.93	7.41	5.35	6.99	1.69	
MnO	5.53	4.73	4.58	3.81	0.64	0.17	0.14	0.17	0.1	0.29	0.57	0.36	0.24	
CaO	1.59	1.26	1.14	1.15	7.08	0	0	0	0	0.02	0.18	0.03	0.01	
Na ₂ O	0	0.04	0.02	0.01	0.02	0.21	0.19	0.18	0.26	0.35	0.37	0.23	0.03	
K ₂ O	0	0	0	0	0	9.66	9.71	9.6	8.55	0.02	0.16	0	0	
Total	100.4	100.03	100.09	99.82	101.23	95.35	95.87	95.36	95.1	99.3	96.94	97.29	98.29	
Mole cation														
Si	2.96	2.95	2.96	2.96	3.01	2.44	2.42	2.42	2.58	5.01	4.98	4.99	1.84	
Ti	0	0	0	0	0.01	0.2	0.21	0.18	0.08	0	0	0	0.01	
Al	2	2	2.01	2.01	1.96	1.58	1.56	1.54	1.65	3.98	3.96	3.98	4.19	
Fe	2.17	2.32	2.09	2.26	2.13	1.12	1.28	1.26	1.18	0.81	1.1	0.89	0.8	
Mg	0.38	0.36	0.55	0.42	0.24	0.79	0.64	0.77	1.29	1.13	0.85	1.1	0.18	
Mn	0.38	0.32	0.31	0.26	0.04	0.01	0.01	0.01	0.33	0.03	0.05	0.03	0.01	
Ca	0.14	0.11	0.1	0.1	0.6	0	0	0	0	0	0.02	0	0	
Na	0	0.01	0	0	0	0.03	0.03	0.04	0.04	0.07	0.08	0.05	0	
K	0	0	0	0	0	0.85	0.87	0.86	0.77	0	0.02	0	0	
End-members (%)														
Alm	70.84	74.41	68.54	74.24	70.89	-	-	-	-	-	-	-	-	
Pyr	12.37	11.64	18.09	13.93	8.02	-	-	-	-	-	-	-	-	
Gro	4.49	3.52	3.19	3.26	19.74	-	-	-	-	-	-	-	-	
Spe	12.31	10.43	10.17	8.56	1.35	-	-	-	-	-	-	-	-	
Ann	-	-	-	-	-	58	66	62	42	-	-	-	-	
Fe-Crd	-	-	-	-	-	-	-	-	-	41.05	54.83	43.99	-	
Fe-St	-	-	-	-	-	-	-	-	-	-	-	-	80	

Powell [1998] (revised in Holland and Powell [2003]). Solution models and end-member phases considered in the pseudosection calculation are listed in Table 3. For each sample, the amount of water used in the P-T pseudosections calculations was estimated from T-M(H₂O) pseudosection.

Samples MN6, MN12, and MN13 show similar bulk rock compositions (Table 1). Pseudosection topology shows two major metamorphic reactions with similar P-T location (Figures 14 and 15). Rocks first underwent muscovite-dehydration melting following the reaction:



Reaction (1) is responsible for the main equilibrium assemblage of Bt + Melt + Plg + Kfs + Grt + Sil + Qtz. The second main metamorphic reaction is melt-consuming and occurred on the retrograde path. It is well illustrated by cordierite coronas around garnet (Figure 13), corresponding to the reaction:

Table 3. Solutions Models Used for Pseudosection Calculations and Corresponding Mineral Names and Abbreviations Used in the Text and Figures

Mineral	Abbreviation [Kretz, 1983]	Solution Model	Reference	End-Members
Biotite	Bt	Bio(TCC)	[Tajčmanová et al., 2009]	mts, sdph, east, mnbi, ann, phl, obi
Muscovite	Mu	Mica(SGH)	[Smye et al., 2010]	mu, pa, ma_dqf, cel, fcel
Garnet	Grt	Gt(WPPH)	[White et al., 2005]	spss, alm, py, gr
Cordierite	Cd	hCrd	Perple'X dataset	mnocrd, fcrd, crd, hmncrd, hfcrd, hcrd
Plagioclase	Plg	Pl(h)	[Newton and Haselton, 1981]	an, abh
K-Feldspar	Kfs	San	[Waldbaum and Thompson, 1969]	san, abh
Staurolite	St	St(HP)	Perple'X dataset	mnst, fst,mst
Melt	melt	melt(HP)	[White et al., 2001]	h2oL, fo8L, fa8L, abL, sil8L, anL, kspL, q8L

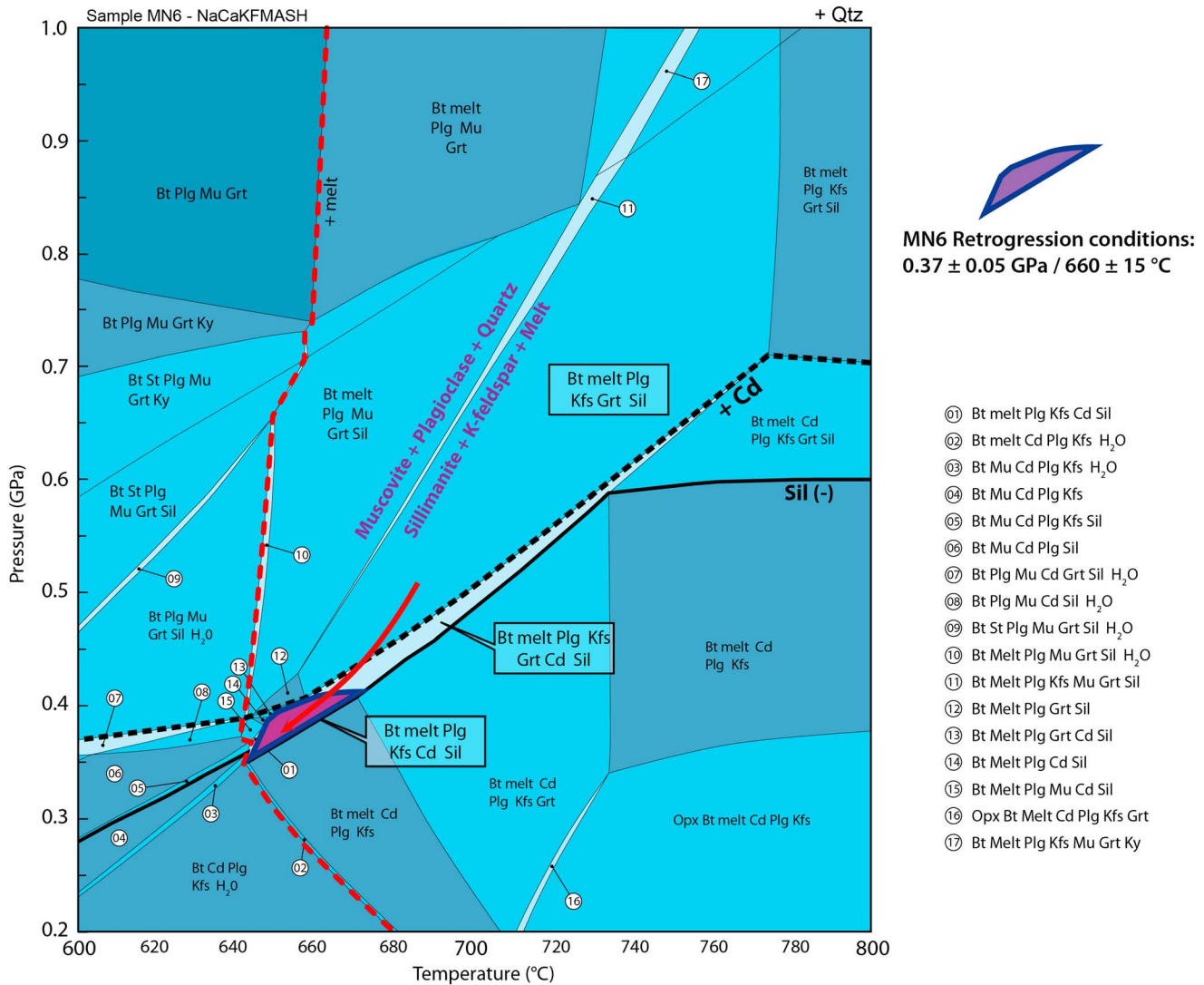


Figure 14. Pseudosection diagram calculated in the MnNCKFASH model for samples MN6 (WGS 84: 43.68558°N; 2.70027°E see location in Figure 1) showing main reactions during the P-T evolution of pelitic metatexite. The mineral abbreviations used are the following: Mu, muscovite; Qtz, quartz; Grt, garnet; Crd, cordierite; St, staurolite; Plg, plagioclase; Kfs, K-feldspar; Bt, biotite; Ky, kyanite; Sil, sillimanite. The solidus curve is represented by the red dotted line, the Crd-in and Sil-out reactions are shown by the black dotted line and plain line, respectively. The resulting P-T evolution for this sample is represented by a red arrow.



This reaction is represented by the assemblage Bt + melt + Plg + Kfs + Grt + Cd + Sil + Qtz. It has a similar position and similar dP/dT slopes in pseudosections for the three samples. This melt-consuming reaction is common in cordierite gneisses [Cenki *et al.*, 2002]. It is considered as a late back-reaction between the restite and the in situ crystallizing melt that resulted in thin cordierite coronas around garnet.

In order to evaluate metamorphic conditions more precisely, the pseudosections for MN6, MN12, and MN13 were contoured for almandine, grossular, annite, and Fe-cordierite molar isopleths in garnet, biotite, and cordierite, respectively. With this approach, the cordierite-bearing assemblage of sample MN6 records P-T conditions culminating at 0.37 ± 0.05 GPa and $660 \pm 15^\circ\text{C}$. Sample MN12 records a peak temperature of $710 \pm 20^\circ\text{C}$ at 0.67 ± 0.05 GPa, and retrograde P-T conditions corresponding to the stability field of Bt + Cd + melt + Plg + Kfs + Grt + Sil are at 0.37 ± 0.05 GPa and $670 \pm 20^\circ\text{C}$ (Figures 15a–15c). Sample MN13 records peak temperature at 0.62 ± 0.07 GPa and $725 \pm 20^\circ\text{C}$; retrograde P-T conditions corresponding to the stability field of Bt + Cd + melt + Plg + Kfs + Grt + Sil are at 0.44 ± 0.05 GPa and $685 \pm 25^\circ\text{C}$ (Figures 15d and 15e).

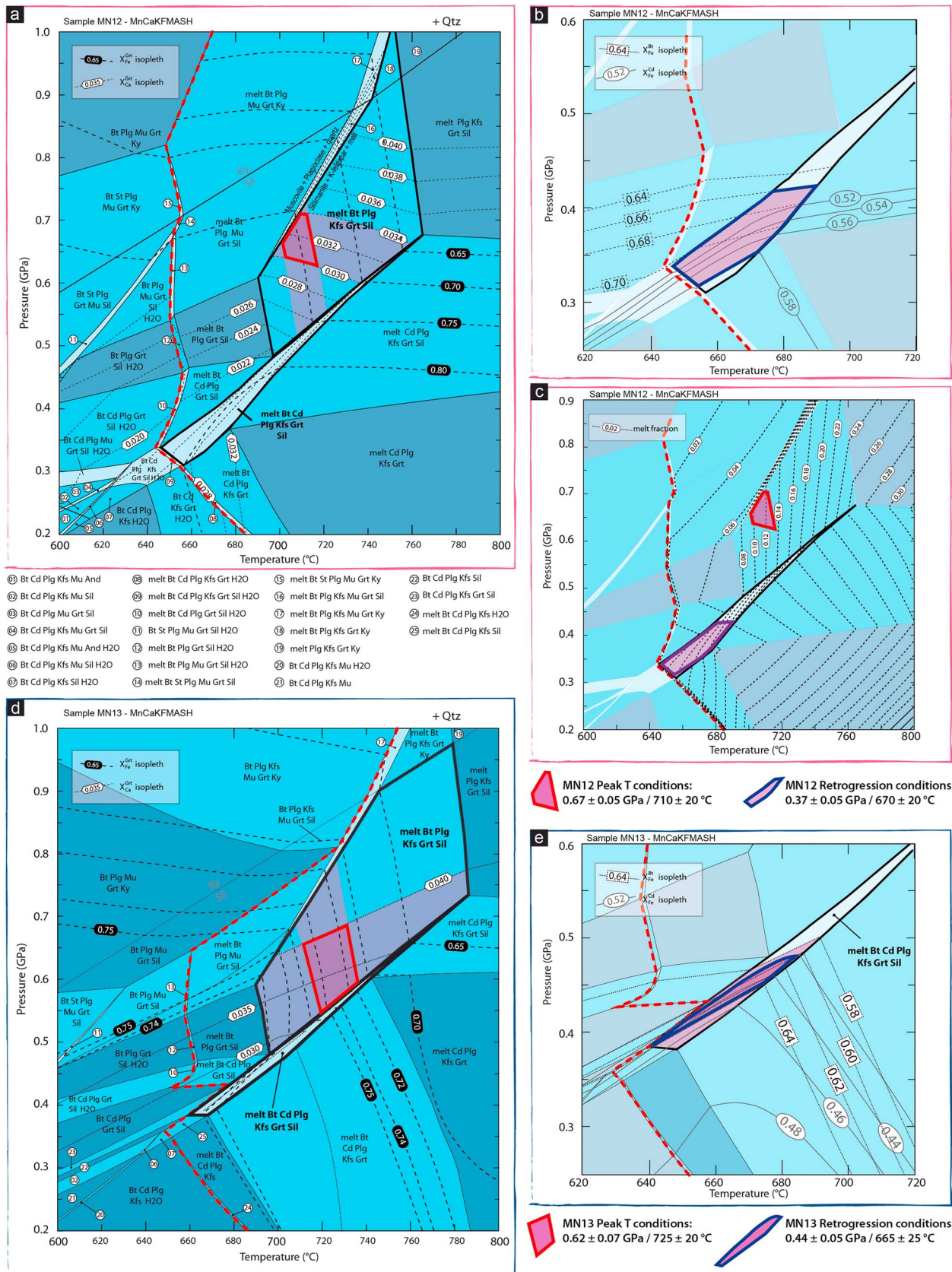


Figure 15

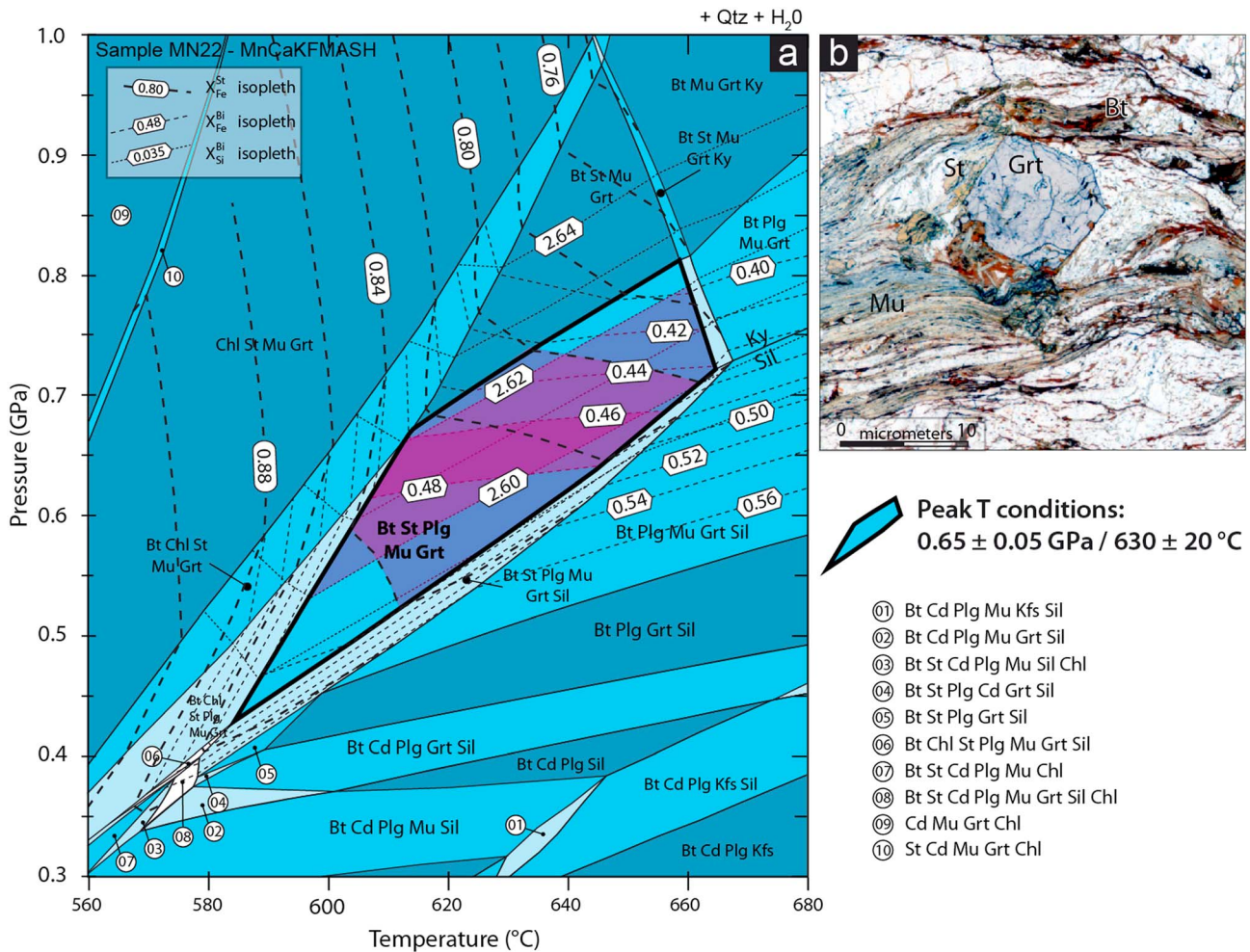


Figure 16. (a) Pseudosection diagrams calculated in the MnNCKFASH system for sample MN22 (WGS 84: 43.51345°N; 2.73991°E). The predicted Bt + Plg + Mu + Grt + St + Qtz-bearing assemblage observed in thin section (microphotograph (b)) gives P-T conditions at 0.65 ± 0.05 GPa and $630 \pm 20^\circ\text{C}$. Compositional isopleths for biotite and staurolite are shown. The isopleth notation used is $X_{\text{Fe}}^{\text{St}} = \text{Fe}/(\text{Fe} + \text{Mg})$, $X_{\text{Si}}^{\text{St}} = \text{Si}/(\text{Si} + \text{Al})$.

In addition to P-T estimates, the percentage of volume of melt produced during metamorphism was calculated for sample MN12 that is representative of an average pelitic composition. According to the predicted P-T evolution (see above), partial melting of metapelite produced a maximum of ~10–12 vol % of melt at peak temperature conditions around 0.6 GPa and 720°C. It is worth noting that this low percentage melt volume value is a minimal approximation because this calculation does not consider melt escape.

Results for sample MN22 are shown in Figure 16. The predicted water saturated stability field of the observed main paragenesis, i.e., biotite + plagioclase + quartz + muscovite + garnet + staurolite ranges from 0.4 to 0.8 GPa and 580 to 660°C. Isopleths for Fe and Si in biotite as well as Fe in staurolite are drawn on MN22 pseudosection (Figure 16). Data are consistent with the three cross-cutting compositional ranges within the Bt + Plg + Qtz + Mu + Grt + St + H₂O stability field. The obtained P-T conditions corresponding to peak temperature assemblage are 0.65 ± 0.05 GPa and $630 \pm 20^\circ\text{C}$.

Figure 15. Pseudosection diagrams calculated in the MnNCKFASH system for samples (a) MN12 (WGS 84: 43.65028°N; 2.74647°E) and (d) MN13 (WGS 84: 43.60144°N; 2.70598°E). (b, e) Zooms show on the right side of the figure highlight the relationships between the different compositional isopleths in the cordierite-bearing assemblage for MN12 and MN13, respectively. (c) Zoom shows the evolution of the melt fraction for MN12 sample. For MN12 sample, peak conditions, and retrograded assemblages are constrained at 0.67 ± 0.05 GPa and $710 \pm 20^\circ\text{C}$, and 0.37 ± 0.05 GPa and $670 \pm 20^\circ\text{C}$, respectively. For MN13 sample, peak conditions and retrograded assemblages are constrained at 0.62 ± 0.07 GPa and $725 \pm 20^\circ\text{C}$, and 0.44 ± 0.05 GPa and $685 \pm 20^\circ\text{C}$, respectively. The end-member mineral abbreviations used are the following: Py, pyrope; Sps, Spessartine; Gro, grossulaire, Gro; Alm, Almandin; the isopleth notation used is $X_{\text{Fe}} = \text{Fe}/(\text{Fe} + \text{Mg})$, $X_{\text{Ca}} = \text{Ca}/(\text{Ca} + \text{Fe} + \text{Mg})$.

5. Discussion

5.1. Is the Montagne Noire Axial Zone a Double Dome?

Based on structural observations on its eastern termination composed of the Espinouse and the Caroux subdomes, the MNAZ was recently described as a double dome [Charles *et al.*, 2009; Rey *et al.*, 2012]. On the other hand, according to Van Den Driessche and Pitra [2012], evidence for the Caroux domal structure is still controversial, and, thus, the double-dome pattern is highly debated. Classically, the general pattern of the Caroux is interpreted as a large E-W trending antiform made of an early synthickening foliation subsequently folded during N-S directed shortening and/or upward displacement of deeper crustal rocks [Faure and Cottureau, 1988; Rey *et al.*, 2011]. In this scheme, Rey *et al.* [2011] consider a high-strain zone that prolongs the Rosis synform toward the west in the core of the dome. Our detailed structural mapping shows a high-strain corridor, defined as D2 HSC, that is not only restricted to the Rosis syncline and its western prolongation but also includes the entire southern part of the Agout dome (Figures 8 and 9). According to our observations, the Caroux massif is located within the D2 high-strain zone. In addition, the top of the Caroux massif is affected by S3 foliation. Therefore, the Caroux dome does not represent a unique foliation envelope folded into a N80° trending isoclinal antiform during one folding event. The finite strain pattern of the Caroux dome is rather considered as a complex heterogeneous structure made by the superposition of at least three distinct planar fabrics S1, S2, and S3.

According to other alternative views, the strain pattern within the Caroux massif is not considered as a dome but results from the upward bending of the footwall (the Caroux gneiss) of an extensional system controlled by a north dipping detachment fault (the Espinouse detachment) located along the northern flank of the Espinouse massif [Van Den Driessche and Brun, 1992; Brun and Van Den Driessche, 1994; Pitra *et al.*, 2012; Van Den Driessche and Pitra, 2012]. The N-S cross sections in the gneiss dome highlight a horizontal strain gradient along the D2 HSC (Figures 7 and 8). A first strain gradient develops northward in the western part of the MNAZ, within the Nore massif (Figures 7a and 7b). Another strain gradient develops southward in the middle and eastern part of the MNAZ, from the Agout massif (Figures 7c and 8). Consequently, the D2 strain gradient observed in the Caroux dome does not develop upward and it is not related to extensional shearing [Van Den Driessche and Pitra, 2012] but probably formed horizontally as suggested by Rey *et al.* [2011].

To conclude, our structural analysis does not favor a double-dome pattern uniquely considering the shapes of the Espinouse and Caroux massifs [Rey *et al.*, 2011]. However, this configuration could be considered at the scale of the entire MNAZ, i.e., considering the whole Agout and Nore massifs. One must keep in mind that the original position of the Nore subdome with respect to the Agout dome remains uncertain. Demange and Jamet [1986] suggested that the Mazamet fault is a Pyrenean reverse fault that may have reworked a late-Variscan dextral strike-slip fault with about 20 km of offset between the two massifs.

5.2. Strain Regime and Strain Partitioning

Within the MNAZ, D1 kinematic indicators are scarce and strong deformation and metamorphism during D2 and D3 make it difficult to decipher D1 kinematics. Nevertheless, the early flat-lying foliation S1 is commonly considered to be related to crustal thickening that occurred after southward nappe stacking [e.g., Matte *et al.*, 1998; Faure *et al.*, 2014].

D2 corresponds to a NW-SE directed horizontal shortening responsible for large-scale folds accompanied by the development of S2 axial planar schistosity. The strong D2 fabric is defined by a steeply dipping to vertical foliation that holds a subhorizontal stretching lineation and along which kinematic criteria indicate a bulk coaxial regime. However, when D2 increases, a dextral component of shearing becomes dominant. The late D2 strain pattern is related to dextral strike-slip shearing with the development of D2 shear zones and shear bands on various scales. Therefore, we suggest that D2 reflects first a NW-SE coaxial compressional regime progressively followed by dextral transpression. This may be consistent with the regional tectonics of the Variscan Ibero-Armorican orocline [Matte and Ribeiro, 1975; Pastor-Galán *et al.*, 2011] with the Montagne Noire massif located along its Eastern branch where dextral transpression predominates.

The D3 strain pattern corresponds to a vertical shortening associated with ENE-SWS horizontal stretching. This deformation is accompanied by a strong vertical finite strain gradient that is upward and downward from the main D3 transition zone that also coincides with the location of the anatectic front as it separates molten from unmolten domains.

Considering D3 stretching within the upper part of the dome core, some authors suggested that the asymmetric character of strain and kinematics at the scale of the dome is evidence for detachment-controlled

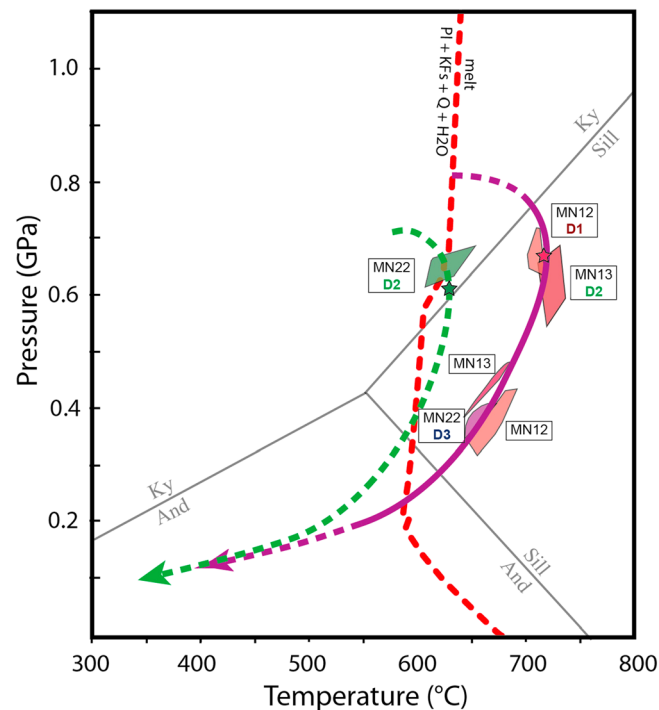


Figure 17. Summary of P-T metamorphic paths recorded by rocks from the MNAZ. The P-T results from this study are shown in red (migmatitic core) and green (adjacent staurolite-garnet-bearing micaschist) colors.

These structural observations indicate a strain partitioning between lower and upper crustal domains synchronous with the development of D2 compressional and D3 extensional deformations in a large-scale dextral transpressional regime. Within the MNAZ, the D2/D3 contemporaneity is manifested by prolate type deformation. L-type tectonites are mainly localized beneath (and within) the S3 transition zone. Similar occurrence of prolate strain patterns resulting from coeval horizontal shortening (D2) and vertical shortening (D3) are described by Franke *et al.* [2011] within the eastern Caroux area and in the southern flank. Numerous observations attesting to an overlap of D2 and D3 in time and space are also reported in the upper crustal levels [Aerden, 1998; Franke *et al.*, 2011]. For instance, in the southern flank of the Montagne Noire massif an ENE-WSW trending extension is documented [Lee *et al.*, 1988; Echtler and Malavieille, 1990; Mattauer *et al.*, 1996] with ENE-WSW directed stretching lineation that parallels a well pronounced crenulation lineation generated by a steeply dipping crenulation cleavage that indicates synchronous NW-SE shortening [Franke *et al.*, 2011].

5.3. Partial Melting-Deformation Feedback Relationship Along the P-T-d-(t) (time) Evolution

Our P-T results emphasize a similar metamorphic evolution for the three samples from the gneissic migmatitic core. Metatexites with a quartz + feldspar + biotite + sillimanite + garnet + cordierite assemblage record a clockwise evolution with peak temperatures around $750 \pm 50^\circ\text{C}$ and 0.65 ± 0.05 GPa, followed by a decompression path with cooling down to $680 \pm 50^\circ\text{C}$ at 0.4 ± 0.1 GPa. The shape of this P-T path is similar to those documented by Soula *et al.* [2001], modified from Ourzik *et al.* [1991], for rocks within the anatexis core (Figure 17). However, our new thermobarometric estimations predict peak temperatures at pressure of about 0.20 GPa to 0.25 GPa higher. Within the micaschist envelope, our results for sample MN22 suggest a peak of metamorphism at 0.65 ± 0.05 GPa and $630 \pm 20^\circ\text{C}$. These P-T conditions are consistent with the structural position of MN22 sample that is adjacent to the anatexis front (Figure 10).

Within the MNAZ orthogneiss and pelitic metatexite units, the main prograde melting reactions are fluid-present congruent and fluid-absent muscovite breakdown dehydration reactions, respectively. The amount of melt produced by these reactions derived from the computed phase diagrams (10–12%, Figure 14c) is consistent with the experimental work that shows that both reactions produce a maximum amount of melt of about 10–15% melt [Castro *et al.*, 2000; Thompson, 1996]. The near-horizontal limit between the lower D2 strain domain and upper D3 strain domain coincides with the anatexis front since migmatization occurred beneath this boundary and not above. Partial melting in response to an increase of internal heat production

gneiss dome development in an extensional setting [Van Den Driessche and Brun, 1992; Brun and Van Den Driessche, 1994; Pitra *et al.*, 2012]. Nevertheless, this assumption is mainly based on the contrasted deformation styles observed only in the eastern MNAZ within orthogneisses along the northern Espinouse and southern Caroux flank [Pitra *et al.*, 2012]. Our work shows that the kinematics in the whole MNAZ is rather symmetric with top-to-the west and top-to-the east shearing along the western and eastern dome terminations, respectively. These observations are consistent with some previous studies [Faure and Cottreau, 1988; Mattauer *et al.*, 1996]. Our study further reveals that this kinematic pattern is mainly focused within the S3 transition zone with some eastward shearing in the central part of the Agout and Nore subdomes.

These structural observations indicate a strain partitioning between lower and upper crustal domains synchronous with the development of D2 compressional and D3 extensional deformations in a large-scale dextral transpressional regime.

after crustal thickening is a common evolution for most collisional orogenic cores. We propose that rocks from the MNAZ core followed a clockwise evolution with peak temperature up to 700°C at around 0.6 GPa (Figure 17). Subsequently, formation of a partially molten middle crust resulted in a dramatic change in force balance and a strong decoupling between the upper and middle crust triggering late-collisional extension, crustal thinning, and orogenic collapse [Vanderhaeghe and Teyssier, 2001; Vanderhaeghe, 2009]. Within the MNAZ, we suggest that incipient melting during prograde metamorphism modified the rheological layering within the Variscan orogenic crust and initiated strain partitioning along the anatectic front. After incipient partial melting, the two domains beneath and above the anatectic front deformed differently with a partition of deformation leading to the appearance of transpressive structures in the lower levels, coeval with along-strike extension in the upper levels.

Looking at the partially molten lower domain (i.e., below the anatectic front), it clearly appears that D2 deformation is localized within the Nore-Somail-Caroux subdomain that is composed of migmatitic orthogneisses. It is likely that due to its mineralogical composition the Caroux orthogneiss may be the first to melt during prograde metamorphism after fluid-present melting at low temperature and thus may have generated a preferential zone of strength weakening along which D2 deformation localized. In this case, the geometry and location of the anatectic front that depends on the bulk composition might vary in space.

Then, the question about the heat source responsible for partial melting in the MNAZ arises. Is the amount of possible crustal thickening sufficient to cause partial melting after thermal relaxation? Is there another heat source? Several occurrences of eclogites are reported within the MNAZ [Demange, 1985; Alabouvette et al., 2003]. The recalculated P-T conditions for the Carbard, Le Jounié, and Terme de Fourcaric eclogites gave minimum peak pressure of approximately 1.4 GPa and a minimum peak temperature of approximately 650–750°C [Franke et al., 2011; Teyssier et al., 2015; Whitney et al., submitted]. Although the precise amount of thickening remains difficult to quantify, one may presume that the orogenic crust thickness reached at least 50 km and probably more. Numerous mafic and ultramafic pods, dismembered dykes, and ultramafic cumulates are also observed within migmatites of the MNAZ [Demange, 1985; Faure et al., 2010]. Some of these mafic rocks are phlogopite-rich dioritic rock that may resemble “vaugnérîtes” that correspond to K-Mg-rich lamprophyres that are widespread in the Massif Central [e.g., Montel and Weisbrod, 1986] in particular within the migmatitic Velay dome located more than 150 km to the northeast.

These mafic intrusions may testify a thermal input from a hot mantle under the orogen that would trigger partial melting and formation of granitic magma. Faure et al. [2014] propose that within the French Variscan belt, a mantle heat input may explain the widespread crustal melting within the middle crust at a continental scale. We suggest that relaxation after crustal thickening together with a mantle input are a likely mechanism to provide the heat necessary to trigger partial melting of the middle crust within the MNAZ.

5.4. Importance of the Anatectic Front as a Rheological Transition Zone

Deformation of the lithosphere subjected to surface and gravity forces is first controlled by three rheological transitions named the brittle-ductile transition zone (BDTZ), the crust-mantle boundary (CMB), and the lithosphere-asthenosphere boundary (LAB). The BDTZ is commonly considered as the main rheological discontinuity acting as the most important decoupling boundary within the orogenic crust [e.g., Kohlstedt et al., 1995]. Within mature orogenic crust, a second main rheological transition arises with the formation of a thick partially molten crustal layer composed of diatexite that behaves as magma [Vanderhaeghe, 2009]. This was experimentally described by Arzi [1978], who first defined the Rheologically Critical Melt Percentage (RCMP) as the rheological transition between mechanical flow controlled by the solid framework of the paleosome to a flow controlled by the melt. Further experimental studies clearly show the existence of the RCMP that would occur between melt fractions of 0.1 to 0.6 depending on experimental conditions [Arzi, 1978; van Der Molen and Paterson, 1979; Rosenberg, 2001]. Alternatively, a reappraisal of experimental work has also pointed out that a few percent of melt is sufficient to reduce considerably the viscosity of partially molten crust [Rosenberg and Handy, 2005]. In nature, this RCMP is strongly dependent on many factors that have not yet been reproduced in experimental studies. These include segregation process and the effect of mechanical anisotropies such as compositional layering. As highlighted by Rosenberg [2001], a rheological transition such as the RMCP probably occurs in nature but is not well defined yet. Our structural and petrological results obtained on the MNAZ show that a strong strain partitioning occurs along the anatectic front (Figure 18). Petrological modeling and field evidence in metatexite, from both metagranite and metapelite,

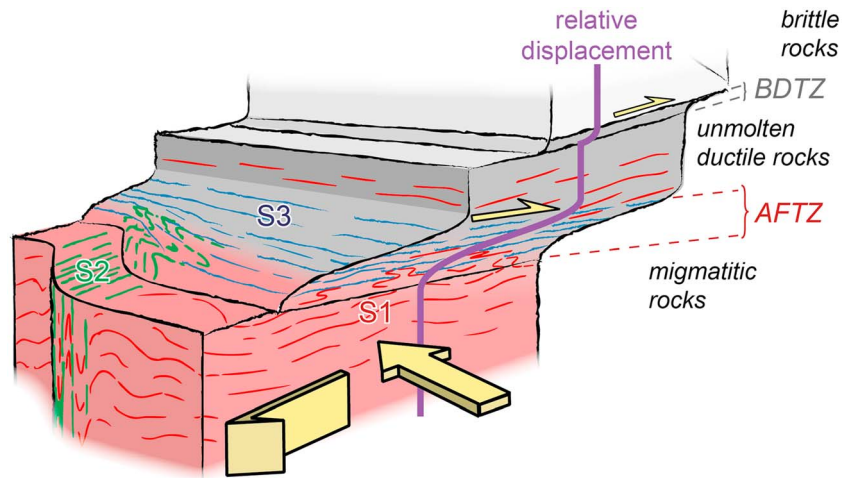


Figure 18. Three-dimensional sketch showing the anatectic front transition zone (AFTZ) as an important rheological boundary within a mature orogenic crust. Based on the case of the MNAZ the three planar fabrics S1, S2, and S3 are represented.

show a relatively low melt fraction. In this part of the late-orogenic Variscan crust, the most prominent location for crustal-scale localization of deformation appears to coincide with the presence of incipient melt (gneiss-metatectite transition) rather than the metatectite-diatectite transition.

In an alternative view *Tikoff et al.* [2004] consider the three major lithospheric rheological boundaries (BDTZ, CMB, and LAB) as attachment zones or clutch zones, emphasizing partial mechanical coupling rather than decoupling. In this “clutch tectonics” model, a clutch zone is defined as a “partial attachment zone between two horizontal lithospheric layers with different displacement fields” [*Tikoff et al.*, 2002]. Thus, a distinction is made with detachment (or decollement, where true decoupling occurs and parts of the crust are subtracted and missing). The concept of “clutch tectonics” and attachment zone is mainly put forward in wrenching, transpression, or transtension settings where displacements between two horizontal lithospheric layers are important but not disrupted [*Tikoff et al.*, 2002; *Zhang and Teyssier*, 2013]. In the MNAZ, coeval development of D2 and D3 with different strain patterns may argue in favor of clutch tectonics in a transpressive setting where the S3 transition zone may represent the top of the attachment zone. *Teyssier and Cruz* [2004] argue that a strong constrictional fabric develops in the upper parts of the transpressive attachment zones owing to combined horizontal and vertical shortening. A similar location of constriction is recorded in the MNAZ and may constitute an argument for “clutch tectonics” in a transpressive regime. Within the MNAZ, a partial attachment zone may act as a coupling zone considering the NW-SE shortening and a decoupling zone considering the SW-NE stretching. *Rey et al.* [2011] interpret the S3 transition zone as a detachment that accommodates eastward escape of the middle crust. The example of the MNAZ demonstrates the importance of considering crustal dynamics as a three-dimensional dynamic system, where coupling during NW-SE shortening may be coeval with decoupling, vertical thinning, and extension in a SW-NE direction. We suggest that tectonic forcing in the deep crust is balanced by orogen-parallel flow in the upper crust. The tectonic forcing leading to strong contraction under transpressive regime in the deep level would be due to crustal indentation [*Culshaw et al.*, 2006]. This is invoked to explain similar structural evolution along the eastern Variscan belt within the Bohemian massif [*Jeřábek et al.*, 2012; *Maierová et al.*, 2014; *Schulmann et al.*, 2014]. In the upper part, orogen-parallel flow assisted by gravitational collapse produces strike-slip structures with subsequent development of pull-apart basin and E-W extension [*Franke et al.*, 2011; *Roger et al.*, 2015].

6. Conclusion

The dome shape and the finite strain pattern of the Montagne Noire Axial Zone (MNAZ) result from the superposition of three deformations D1, D2, and D3. Our petrological results yield a typical clockwise P-T-d-t path, along which rocks from the middle crust experienced partial melting at the end of their prograde evolution. In the MNAZ, the anatectic front is the most relevant rheological boundary within the late-orogenic crust. After incipient partial melting, strain partitioned into transpression and along-strike extension beneath

and above the anatexis front, respectively. Further work is needed to improve understanding of the tectonothermal evolution of the MNAZ and partial melting-deformation feedback relationships within the crust. In particular, in situ dating of synkinematic minerals is essential in order to unravel rates of metamorphic and tectonic processes associated to gneiss dome formation.

Acknowledgments

This research was financially supported by SRO program from the Observatoire des Sciences de l'Univers Theta, University of Franche-Comté and an INSU/SYSTER project from French CNRS. The structural and petrological data for this paper are available by contacting the corresponding author, Mickael Rabin (mickael.rabin@univ-fcomte.fr) or the second author, Pierre Trap (pierre.trap@univ-fcomte.fr). We thank the three anonymous reviewers for their fruitful comments.

References

- Aerden, D. (1998), Tectonic evolution of the Montagne Noire and a possible orogenic model for syncollisional exhumation of deep rocks, Variscan belt, France, *Tectonics*, 17(1), 62–79, doi:10.1029/97TC02342.
- Alabouvette, B., and M. Demange (1993), Carte géologique de la France (1/50000) feuille de Saint-Pons (1013), BRGM, Orléans, France.
- Alabouvette, B., M. Demange, J. Guérangé-Lozes, and P. Ambert (2003), Notice et carte géologique de la France (1/250000) feuille de Montpellier, BRGM, Orléans, France.
- Arthaud, F. (1970), *Étude tectonique et microtectonique comparée de deux domaines hercyniens: Les Nappes de la Montagne Noire (France) et L'anticlinorium de l'Iglesiente (Sardaigne): Style des Déformations Successives, Notions de Sous-Faciès de Faciès et de Profils Tectoniques*, Univ. des Sciences et Techniques du Languedoc (USTELA), Montpellier, France.
- Arzi, A. (1978), Critical phenomena in rheology of partially melted rocks, *Tectonophysics*, 44(1–4), 173–184, doi:10.1016/0040-1951(78)90069-0.
- Ballèvre, M., S. Fourcade, R. Capdevila, J. J. Peucat, A. Cocherie, and C. Mark Fanning (2012), Geochronology and geochemistry of Ordovician felsic volcanism in the Southern Armorican Massif (Variscan belt, France): Implications for the breakup of Gondwana, *Gondwana Res.*, 21, 1019–1036.
- Bard, J. (1978), New interpretation of origin and relative age of augengneisses in Axial Zone of Montagne Noire and its tectonic consequences, *C. R. Hebd. Seances Acad. Sci. Ser. D*, 287(2), 65–68.
- Bard, J.-P., and R. Rambeloson (1973), Métamorphisme plurifacial et sens de variation du degré géothermique durant la tectogenèse polyphasée hercynienne dans la partie orientale de la zone axiale de la Montagne Noire (Massif du Caroux, Sud du Massif Central français), *Bull. Soc. Géol. Fr.*, 7(5–6), 579–586.
- Be Mezeme, E. (2005), Contribution de la géochronologie U-Th-Pb sur monazite à la compréhension de la fusion crustale dans la chaîne varisque française et implication géodynamique, PhD thesis, Univ. d'Orléans, Orléans, France.
- Beaud, F. (1985), Etude structurale de la zone axiale orientale de la Montagne Noire (sud du Massif central français): Détermination des mécanismes de déformation; relation avec les nappes du versant sud = Structural analysis of the eastern Axial Zone of the Montagne Noire (South of French Massif Central), Determination of the deformation mechanisms related to the thrusts of the southern slope. [Available at <http://cat.inist.fr/?aModele=afficheN&cpsid=8695101> (Accessed 16 May 2014).]
- Bergeron, J. (1905), The tectonics of the region situated in the north of the Montagne Noire, *C. R. Hebd. Seances Acad. Sci.*, 140, 466–467.
- Bogdanoff, S., M. Donnot, and F. Ellenberger (1984), Notice et carte géologique de la France (1/50000) feuille de Bédarieux (988), BRGM, Orléans.
- Bouchardon, J., R. Dechomets, and M. Demange (1979), Kyanite in micaschists and gneisses from synclinal de Rosis and flanc sud de la Montagne Noire (French Massif Central), *C. R. Hebd. Seances Acad. Sci. Ser. D*, 288, 1067–1069.
- Brun, J.-P., and J. Van Den Driessche (1994), Extensional gneiss domes and detachment fault systems; structure and kinematics, *Bull. Soc. Geol. Fr.*, 165(6), 519–530.
- Cassard, D., J. Feybesse, and J. Lescuyer (1993), Variscan crustal thickening, extension and late overstacking during the Namurian Westphalian in the western Montagne Noire (France), *Tectonophysics*, 222(1), 33–53, doi:10.1016/0040-1951(93)90188-P.
- Castro, A., L. G. Corretgé, M. El-Biad, H. El-Hmidi, C. Fernández, and A. E. P. Douce (2000), Experimental constraints on Hercynian Anatexis in the Iberian Massif, Spain, *J. Petrol.*, 41(10), 1471–1488, doi:10.1093/petrology/41.10.1471.
- Seni, B., L. M. Kriegsman, and I. Braun (2002), Melt-producing and melt-consuming reactions in the Achankovil cordierite gneisses, South India, *J. Metamorph. Geol.*, 20(6), 543–561, doi:10.1046/j.1525-1314.2002.00388.x.
- Charles, N., M. Faure, and Y. Chen (2009), The Montagne Noire migmatitic dome emplacement (French Massif Central): New insights from petrofabric and AMS studies, *J. Struct. Geol.*, 31(11), 1423–1440, doi:10.1016/j.jsg.2009.08.007.
- Cocherie, A., T. Baudin, A. Autran, C. Guerrot, C. M. Fanning, and B. Laumonier (2005), U-Pb zircon (ID-TIMS and SHRIMP) evidence for the early Ordovician intrusion of metagranites in the late Proterozoic Canaveilles Group of the Pyrenees and the Montagne Noire (France), *Bull. Soc. Geol. Fr.*, 176(3), 269–282, doi:10.2113/176.3.269.
- Collomb, P., and F. Ellenberger (1965), Age Relatif Et Signification De La Ligneation Regionale Dans La Montagne Noire (massif Du Caroux Et Ses Enveloppes Herault), *C. R. Hebd. Seances Acad. Sci.*, 261(1), 195–199.
- Collot, B. (1980), Les filons apalto-pegmatitiques du massif du Caroux (Montagne Noire): Déformation et mécanismes de mise en place, *Bull. BRGM*, 2, 257–267.
- Connolly, J. A. D. (2005), Computation of phase equilibria by linear programming: A tool for geodynamic modeling and its application to subduction zone decarbonation, *Earth Planet. Sci. Lett.*, 236(1–2), 524–541, doi:10.1016/j.epsl.2005.04.033.
- Connolly, J. A. D., and K. Petrini (2002), An automated strategy for calculation of phase diagram sections and retrieval of rock properties as a function of physical conditions, *J. Metamorph. Geol.*, 20(7), 697–708, doi:10.1046/j.1525-1314.2002.00398.x.
- Courtilot, V., P. Chambon, J. Brun, P. Rochette, and P. Matte (1986), A magnetotectonic study of the Hercynian Montagne Noire (France), *Tectonics*, 5(5), 733–751, doi:10.1029/TC005i005p00733.
- Culshaw, N. G., C. Beaumont, and R. A. Jamieson (2006), The orogenic superstructure-infrastructure concept: Revisited, quantified, and revived, *Geology*, 34, 733–736.
- Debat, P. (1967), Etude Petrographique Des Gneiss Oeilles Intercalés Dans La Serie Micaschisteuse Du Sorezois (Montagne Noire), *Bull. Soc. Fr. Mineral. Cristallogr.*, 90(2), 236–240.
- Debat, P., and M. P. Mouline (1979), Carte géologique de la France (1/50000) feuille de Mazamet (1012), BRGM, Orléans, France.
- Demange, M. (1975), Pennic style of Axial Zone of Montagne Noire (Massif Central, France), *C. R. Hebd. Seances Acad. Sci. Ser. D*, 280(1), 5–8.
- Demange, M. (1982), Etude Géologique du Massif de l'Agout, Thesis, Paris VI, Montagne Noire, France.
- Demange, M. (1985), The eclogite-facies rocks of the Montagne-Noire, France, *Chem. Geol.*, 50, 173–188, doi:10.1016/0009-2541(85)90119-6.
- Demange, M. (1993), What does the Monts-De-Lacaune Fault (Montagne-Noire, France) mean—Implications for the origin of the Nappes, *C. R. Acad. Sci. Ser. II*, 317(3), 411–418.
- Demange, M. (1994a), Antevariscan evolution of the Montagne-Noire (France)—From a passive margin to a foreland basin, *C. R. Acad. Sci. Ser. II*, 318(7), 921–933.

- Demange, M. (1994b), Sorezois—A key point for an understanding of relations between the Axial Zone and the Variscan Nappes of Montagne-Noire (France), *C. R. Acad. Sci. Ser. II*, *318*(11), 1543–1549.
- Demange, M. (1996), Extensional gneiss domes and detachment fault systems: Structure and kinematics—Observations and remarks, *Bull. Soc. Geol. Fr.*, *167*(2), 295–298.
- Demange, M. (1998), Contribution au problème de la formation des dômes de la Zone axiale de la Montagne Noire: Analyse géométrique des plissements superposés dans les séries métasédimentaires de l'enveloppe. Implications pour tout modèle géodynamique, *Géol. Fr.*, *4*, 3–56.
- Demange, M. (1999), Evolution tectonique de la Montagne Noire: Un modèle en transpression, *C. R. Acad. Sci. Ser. IIA Earth Planet. Sci.*, *329*(11), 823–829, doi:10.1016/S1251-8050(00)88638-3.
- Demange, M., and P. Jamet (1986), L'accident majeur Mazamet-Tantajo (Montagne Noire): Décrochement tardihercynien et faille inverse pyrénéenne, *Géol. Fr.*, *3*, 273–280.
- Demange, M., J. Guérangé-Lozes, and B. Guérangé (1995), Carte géologique de la France (1/50000) feuille de Lacauze (987), BRGM, Orléans.
- Demange, M., B. Alabouvette, M. P. Mouline, and J. G. Astrac (1997), Carte géologique de la France (1/50000) feuille de Revel (1011), BRGM, Orléans.
- Denèle, Y., B. Laumonier, J.-L. Paquette, P. Olivier, G. Gleizes, and P. Barbey (2014), Timing of granite emplacement, crustal flow and gneiss dome formation in the Variscan segment of the Pyrenees, *Spec. Publ.-Geol. Soc. London*, *405*, 265–287, doi:10.1144/SP405.5.
- Denizot, G. (1954), La Tectonique De La Montagne-Noire Et Lennoyage De Lorb, Autour De Roquebrun (Herauld), *C. R. Hebd. Seances Acad. Sci.*, *238*(20), 2007–2008.
- Doublier, M. P., S. Potel, and K. Wemmer (2014), The tectono-metamorphic evolution of the very low-grade hanging wall constrains two stage gneiss dome formation in the Montagne Noire example (S-France), *J. Metamorph. Geol.*, 71–89, doi:10.1111/jmg.12111.
- Echtler, H., and J. Malavieille (1990), Extensional tectonics, basement uplift and Stephano-Permian Collapse basin in a late Variscan metamorphic core complex (Montagne Noire, Southern Massif-Central), *Tectonophysics*, *177*(1–3), 125–138, doi:10.1016/0040-1951(90)90277-F.
- Faure, M., and N. Cottreau (1988), Kinematic data on the emplacement of the Middle Carboniferous migmatitic dome in the Axial Zone of the Montagne Noire (Massif Central, France), *C. R. Acad. Sci. Ser. II*, *307*(16), 1787–1794.
- Faure, M., J. M. Lardeaux, and P. Ledru (2009), A review of the pre-Permian geology of the Variscan French Massif Central, *C. R. Geosci.*, *341*, 202–213.
- Faure, M., A. Cocherie, E. B. Mezeme, N. Charles, and P. Rossi (2010), Middle Carboniferous crustal melting in the Variscan belt: New insights from U-Th-Pb-tot monazite and U-Pb zircon ages of the Montagne Noire Axial Zone (southern French Massif Central), *Gondwana Res.*, *18*(4), 653–673, doi:10.1016/j.gr.2010.02.005.
- Faure, M., A. Cocherie, J. Gaché, C. Esnault, C. Guerrot, P. Rossi, L. Wei, and L. Qiuli (2014), Middle Carboniferous intracontinental subduction in the Outer Zone of the Variscan belt (Montagne Noire Axial Zone, French Massif Central): Multimethod geochronological approach of polyphase metamorphism, *Spec. Publ.-Geol. Soc. London*, *405*, 289–311, doi:10.1144/SP405.2.
- Feist, R., and J. Galtier (1985), Discovery of a probable Namurian age flora in the Olistolitic Flysch of Cabrières (Herauld)—Significance on the duration of the synorogenic sedimentation in the Montagne Noire (southern France), *C. R. Acad. Sci. Ser. II*, *300*(6), 207–212.
- Feybesse, J. L., J. M. Lardeaux, V. Johan, M. Tegyej, E. Dufour, B. Lemiere, and J. Delfour (1988), La série de la Brèvenne (Massif Central France): Une unité dévonienne charriée sur le complexe métamorphique des Monts du Lyonnais à la fin de la collision varisque, *C. R. Acad. Sci. Paris*, *307*, 991–996.
- Franke, W., M. P. Doublier, K. Klama, S. Potel, and K. Wemmer (2011), Hot metamorphic core complex in a cold foreland, *Int. J. Earth Sci.*, *100*(4), 753–785, doi:10.1007/s00531-010-0512-7.
- Geze, B. (1940), On the orogenic phases and metamorphism in the Montagne Noire, *C. R. Hebd. Seances Acad. Sci.*, *211*, 403–406.
- Gèze, B. (1949), *Etude Géologique de la Montagne Noire et des Cévennes Méridionales*, Société géologique, Paris.
- Hamet, J., and C. Allegre (1976), Hercynian orogeny in Montagne Noire (France)—Application of Rb-87-Sr-87 systematics, *Geol. Soc. Am. Bull.*, *87*(10), 1429–1442, doi:10.1130/0016-7606(1976)87<1429:HOITMN>2.0.CO;2.
- Holland, T. J. B., and R. Powell (1998), An internally consistent thermodynamic data set for phases of petrological interest, *J. Metamorph. Geol.*, *16*(3), 309–343, doi:10.1111/j.1525-1314.1998.00140.x.
- Holland, T., and R. Powell (2003), Activity–composition relations for phases in petrological calculations: An asymmetric multicomponent formulation, *Contrib. Mineral. Petrol.*, *145*(4), 492–501, doi:10.1007/s00410-003-0464-z.
- Jansen, J. B. H., and R. D. Schuiling (1976), Metamorphism on Naxos; petrology and geothermal gradients, *Am. J. Sci.*, *276*(10), 1225–1253, doi:10.2475/ajs.276.10.1225.
- Jeřábek, P., O. Lexa, K. Schulmann, and D. Plašienka (2012), Inverse ductile thinning via lower crustal flow and fold-induced doming in the West Carpathian Eo-Alpine collisional wedge, *Tectonics*, *31*, TC5002, doi:10.1029/2012TC003097.
- Johnston, S. T., and G. Gutierrez-Alonso (2010), The North American Cordillera and West European Variscides: Contrasting interpretations of similar mountain systems, *Gondwana Res.*, *17*(2–3), 516–525, doi:10.1016/j.gr.2009.11.006.
- Kohlstedt, D. L., B. Evans, and J. S. Mackwell (1995), Strength of the lithosphere: Constraints imposed by laboratory experiments, *J. Geophys. Res.*, *100*, 17,587–17,602, doi:10.1029/95JB01460.
- Kretz, R. (1983), Symbols for rock-forming minerals, *Am. Mineral.*, *68*, 277–279.
- Kruckenberger, S. C., O. Vanderhaeghe, E. C. Ferre, C. Teyssier, and D. L. Whitney (2011), Flow of partially molten crust and the internal dynamics of a migmatite dome, Naxos, Greece, *Tectonics*, *30*, TC3001, doi:10.1029/2010TC002751.
- Lardeaux, J. M., K. Schulmann, M. Faure, V. Janoušek, O. Lexa, E. Skrzypczek, J. B. Edel, and P. Štípská (2014), The Moldanubian zone in the French Massif Central, Vosges/Schwarzwald and Bohemian Massif revisited: Differences and similarities, *Geol. Soc. London Spec. Publ.*, *405*, 7–44, doi:10.1144/SP405.14.
- Laumonier, B., A. Autran, P. Barbey, A. Cheilletz, T. Baudin, A. Cocherie, and C. Guerrot (2004), On the non-existence of a Cadomian basement in southern France (Pyrenees, Montagne Noire): Implications for the significance of the pre-Variscan (pre-Upper Ordovician) series, *Bull. Soc. Geol. Fr.*, *175*(6), 643–655, doi:10.2113/175.6.643.
- Lee, B., M. Faure, D. Cluzel, and J. Cadet (1988), Evidence for a ductile shearing from west to east in the Nappes of the southern side of the Montagne Noire (southern Massif Central, France), *C. R. Acad. Sci. Ser. II*, *306*(6), 455–462.
- Maierová, P., O. Lexa, K. Schulmann, and P. Štípská (2014), Contrasting tectonic and metamorphic evolution of orogenic lower crust in the Bohemian Massif: A numerical model, *Gondwana Res.*, *25*(2), 509–521.
- Malavieille, J. (2010), Impact of erosion, sedimentation, and structural heritage on the structure and kinematics of orogenic wedges: Analog models and case studies, *Geol. Soc. Am.*, 4–10, doi:10.1130/GSATG48A.1.
- Marres, P. (1951), La géologie de la Montagne Noire et des Cévennes méridionales, *Ann. Géogr.*, *60*(321), 281–285, doi:10.3406/geo.1951.13275.

- Mattauer, M., P. Laurent, and P. Matte (1996), Post-nappe syn-cleavage Hercynian folding and horizontal stretching in the southern part of Montagne Noire (Southern Massif Central, France), *C. R. Acad. Sci. Ser. II Fasc. -Sci.*, *322*(4), 309–315.
- Matte, P. (1991), Accretionary history and crustal evolution of the Variscan belt in Western-Europe, *Tectonophysics*, *196*(3–4), 309–337, doi:10.1016/0040-1951(91)90328-P.
- Matte, P. (2001), The Variscan collage and orogeny (480–290 Ma) and the tectonic definition of the Armorica microplate: A review, *Terra Nova*, *13*(2), 122–128, doi:10.1046/j.1365-3121.2001.00327.x.
- Matte, P., and A. Ribeiro (1975), Forme et orientation de l'ellipsoïde de déformation dans la virgation Hercynienne de Galice. Relations avec le plissement et hypothèses sur la genèse de l'arc Ibéro-Armoricain, *C. R. Acad. Sci. Ser. D*, *280*, 2825–2828.
- Matte, P., J. Lancelot, and M. Mattauer (1998), The Montagne Noire Hercynian Axial Zone is not an extensional metamorphic core complex but a compressional post-nappe anticline with an anatectic core, *Geodinamica Acta*, *11*(1), 13–22, doi:10.1016/S0985-3111(98)80025-9.
- Melleton, J., A. Cocherie, M. Faure, and P. Rossi (2010), Precambrian protoliths and Early Paleozoic magmatism in the French Massif Central: U-Pb data and the North Gondwana connection in the west European Variscan belt, *Gondwana Res.*, *17*(1), 13–25, doi:10.1016/j.jgr.2009.05.007.
- Montel, J. M., and A. Weisbrod (1986), Characteristics and evolution of 'vaugneritic magmas', an analytical and experimental approach on the example of the Cévennes Médiannes (French Massif Central), *Bull. Mineral.*, *109*, 575–587.
- Newton, R. C., and H. T. Haselton (1981), Thermodynamics of the garnet—plagioclase— Al_2SiO_5 —quartz geobarometer, in *Thermodynamics of Minerals and Melts*, *Adv. Phys. Geochem.*, vol. 1, edited by R. C. Newton, A. Navrotsky, and B. J. Wood, pp. 131–147, Springer, New York.
- Norlander, B. H., D. L. Whitney, C. Teyssier, and O. Vanderhaeghe (2002), Partial melting and decompression of the Thor-Odin dome, Shuswap metamorphic core complex, Canadian Cordillera, *Lithos*, *61*(3–4), 103–125, doi:10.1016/S0024-4937(02)00075-0.
- Ourzik, A., P. Debat, and A. Mercier (1991), Metamorphic evolution of the N and Ne parts of the Montagne Noire Axial Zone (southern Massif-Central, France), *C. R. Acad. Sci. Ser. II*, *313*(13), 1547–1553.
- Pastor-Galán, D., G. Gutiérrez-Alonso, and A. B. Weil (2011), Orocline timing through joint analysis: Insights from the Ibero-Armorican Arc, *Tectonophysics*, *507*(1–4), 31–46, doi:10.1016/j.tecto.2011.05.005.
- Pitra, P., M. Pujol, J. Van Den Driessche, J.-C. Poilvet, and J.-L. Paquette (2012), Early Permian extensional shearing of an Ordovician granite: The Saint-Eutrope "C/S-like" orthogneiss (Montagne Noire, French Massif Central), *C. R. Geosci.*, *344*(8), 377–384, doi:10.1016/j.crte.2012.06.002.
- Poilvet, J.-C., M. Pujol, P. Pitra, J. Van den Driessche, and J.-L. Paquette (2011), The Montalet granite, Montagne Noire, France: An Early Permian syn-extensional pluton as evidenced by new U-Th-Pb data on zircon and monazite, *C. R. Geosci.*, *343*(7), 454–461, doi:10.1016/j.crte.2011.06.002.
- Rey, P. F., C. Teyssier, S. C. Kruckenberg, and D. L. Whitney (2011), Viscous collision in channel explains double domes in metamorphic core complexes, *Geology*, *39*(4), 387–390, doi:10.1130/G31587.1.
- Rey, P. F., C. Teyssier, S. C. Kruckenberg, and D. L. Whitney (2012), Viscous collision in channel explains double domes in metamorphic core complexes: REPLY, *Geology*, *40*(10), e280–e280, doi:10.1130/G33202Y.1.
- Robardet, M., F. Paris, and P. R. Racheboeuf (1990), Palaeogeographic evolution of southwestern Europe during Early Palaeozoic times, *Geol. Soc. London Mem.*, *12*(1), 411–419, doi:10.1144/GSL.MEM.1990.012.01.38.
- Roger, F., J.-P. Respaut, M. Brunel, P. Matte, and J.-L. Paquette (2004), Première datation U-Pb des orthogneiss ocellés de la zone axiale de la Montagne Noire (Sud du Massif central): Nouveaux témoins du magmatisme ordovicien dans la chaîne Varisque, *C. R. Geosci.*, *336*(1), 19–28, doi:10.1016/j.crte.2003.10.014.
- Roger, F., C. Teyssier, J. P. Respaut, P. F. Rey, M. Jolivet, D. L. Whitney, J. L. Paquette, and M. Brunel (2015), Timing of formation and exhumation of the Montagne Noire double dome, French Massif Central, *Tectonophysics*, *640–641*(20), 53–69.
- Rosenberg, C. L. (2001), Deformation of partially-molten granite: A review and comparison of experimental and natural case studies, *Int. J. Earth Sci.*, *90*, 60–76.
- Rosenberg, C. L., and M. R. Handy (2005), Experimental deformation of partially melted granite revisited: Implications for the continental crust, *J. Metamorph. Geol.*, *23*(1), 19–28, doi:10.1111/j.1525-1314.2005.00555.x.
- Schilling, R. D. (1960), *Le dôme Gneissique de l'Agout (Tarn et Hérault)*, Société Géologique de France, Paris.
- Schulmann, K., J.-E. Martelat, S. Ulrich, O. Lexa, P. Štípská, and J. K. Becker (2008), Evolution of microstructure and melt topology in partially molten granitic mylonite: Implications for rheology of felsic middle crust, *J. Geophys. Res.*, *113*, B10406, doi:10.1029/2007JB005508.
- Schulmann, K., O. Lexa, V. Janoušek, J. M. Lardeaux, and J. B. Edl (2014), Anatomy of a diffuse cryptic suture zone: An example from the Bohemian Massif, European Variscides, *Geology*, *42*(4), 275–278.
- Smye, A. J., L. V. Greenwood, and T. J. B. Holland (2010), Garnet—chloritoid—kyanite assemblages: Eclogite facies indicators of subduction constraints in orogenic belts, *J. Metamorph. Geol.*, *28*(7), 753–768, doi:10.1111/j.1525-1314.2010.00889.x.
- Soula, J. C., P. Debat, S. Brusset, G. Bessiere, F. Christophoul, and J. Deramond (2001), Thrust-related, diapiric, and extensional doming in a frontal orogenic wedge: Example of the Montagne Noire, Southern French Hercynian belt, *J. Struct. Geol.*, *23*(11), 1677–1699, doi:10.1016/S0191-8141(01)00021-9.
- Tait, J. A., V. Bachtadse, W. Franke, and H. C. Soffel (1997), Geodynamic evolution of the European Variscan fold belt: Palaeomagnetic and geological constraints, *Geol. Rundsch.*, *86*(3), 585–598, doi:10.1007/s005310050165.
- Tajčmanová, L., J. A. D. Connolly, and B. Cesare (2009), A thermodynamic model for titanium and ferric iron solution in biotite, *J. Metamorph. Geol.*, *27*(2), 153–165, doi:10.1111/j.1525-1314.2009.00812.x.
- Teyssier, C., and L. Cruz (2004), Strain gradients in transpressional to transtensional attachment zones, in *Vertical Coupling and Decoupling in the Lithosphere*, vol. 227, edited by J. Grocott et al., pp. 101–115, Geol. Soc. House, Bath, U. K.
- Teyssier, C., D. L. Whitney, F. Roger, P. Rey, and P. Trap (2015), Coeval eclogitization and migmatization during orogenic collapse (Montagne Noire dome), Oral presentation in Variscan Special Meeting, Rennes, France.
- Thompson, A. B. (1996), Fertility of crustal rocks during anatexis, *Trans. R. Soc. Edinburgh: Earth Sci.*, *87*, 1–10.
- Thompson, P., and J. Bard (1982), Isograds and mineral assemblages in the eastern Axial Zone, Montagne Noire (France)—Implications for temperature-gradients and P-T history, *Can. J. Earth Sci.*, *19*(1), 129–143.
- Tikoff, B., C. Teyssier, and C. Waters (2002), Clutch tectonics and the partial attachment of lithospheric layers, *EGU Stephan Mueller Spec. Publ. Ser.*, *1*, 57–73.
- Tikoff, B., R. Russo, C. Teyssier, and A. Tommasi (2004), Mantle-driven deformation of orogenic zones and clutch tectonics, in *Vertical Coupling and Decoupling in the Lithosphere*, vol. 227, edited by J. Grocott et al., pp. 41–64, Geol. Soc. House, Bath.
- Van Den Driessche, J., and J. P. Brun (1992), Tectonic evolution of the Montagne Noire (French Massif Central): A model of extensional gneiss dome, *Geodinamica Acta*, *5*, 85–101.

- Van Den Driessche, J., and P. Pitra (2012), Viscous collision in channel explains double domes in metamorphic core complexes: COMMENT, *Geology*, *40*(10), e279–e279, doi:10.1130/G32727C.1.
- Vanderhaeghe, O. (2009), Migmatites, granites and orogeny: Flow modes of partially-molten rocks and magmas associated with melt/solid segregation in orogenic belts, *Tectonophysics*, *477*(3–4), 119–134, doi:10.1016/j.tecto.2009.06.021.
- Vanderhaeghe, O. (2012), The thermal–mechanical evolution of crustal orogenic belts at convergent plate boundaries: A reappraisal of the orogenic cycle, *J. Geodyn.*, *56–57*, 124–145, doi:10.1016/j.jog.2011.10.004.
- Vanderhaeghe, O., and C. Teyssier (2001), Partial melting and flow of orogens, *Tectonophysics*, *342*(3–4), 451–472, doi:10.1016/S0040-1951(01)00175-5.
- van Der Molen, I., and M. S. Paterson (1979), Experimental deformation of partially melted granite, *Contrib. Mineral. Petrol.*, *70*, 299–318.
- Vidal, J., L. Kubin, P. Debat, and J. Soula (1980), Deformation and dynamic recrystallization of K-feldspar augen in orthogneiss from Montagne-Noire, Occitania, Southern France, *Lithos*, *13*(3), 247–255, doi:10.1016/0024-4937(80)90070-5.
- Von Raumer, J. F., F. Bussy, and G. M. Stampfli (2009), The Variscan evolution in the External massifs of the Alps and place in their Variscan framework, *C. R. Geosci.*, *341*(2–3), 239–252, doi:10.1016/j.crte.2008.11.007.
- Waldbaum, D. R., and J. B. Thompson (1969), Mixing properties of sanidine crystalline solutions: IV. Phase diagrams from equations of state, *Am. Mineral.*, *54*(9–10), 1274–1298.
- White, R. W., R. Powell, and T. J. B. Holland (2001), Calculation of partial melting equilibria in the system Na₂O–CaO–K₂O–FeO–MgO–Al₂O₃–SiO₂–H₂O (NCKFMASH), *J. Metamorph. Geol.*, *19*(2), 139–153, doi:10.1046/j.0263-4929.2000.00303.x.
- White, R. W., N. E. Pomroy, and R. Powell (2005), An in situ metatexite–diatexite transition in upper amphibolite facies rocks from Broken Hill, Australia, *J. Metamorph. Geol.*, *23*(7), 579–602, doi:10.1111/j.1525-1314.2005.00597.x.
- Zhang, Q., and C. Teyssier (2013), Flow vorticity in Zhangbaling transpressional attachment zone, SE China, *J. Struct. Geol.*, *48*, 75–84, doi:10.1016/j.jsg.2012.12.006.